INL/JOU-25-83090-Revision-0

Assessment of Irradiation Embrittlement Effect on Fatigue Life of a Pressurized Light Water Reactor Pressure Vessel Using the Fracture Toughness Master Curve Approach

Minh Tran, Ondrej Muransky, Benjamin W Spencer

Changing the World's Energy Future

Idaho National Laboratory

INL is a U.S. Department of Energy National Laboratory operated by Battelle Energy Alliance, LLC

INL/JOU-25-83090-Revision-0

Assessment of Irradiation Embrittlement Effect on Fatigue Life of a Pressurized Light Water Reactor Pressure Vessel Using the Fracture Toughness Master Curve Approach

Minh Tran, Ondrej Muransky, Benjamin W Spencer

July 2025

Idaho National Laboratory
Idaho Falls, Idaho 83415

http://www.inl.gov

Prepared for the
U.S. Department of Energy
Under DOE Idaho Operations Office
Contract DE-AC07-05ID14517

Nuclear Engineering and Design 443 (2025) 114269

Contents lists available at ScienceDirect

Nuclear Engineering and Design

journal homepage: www.elsevier.com/locate/nucengdes

Assessment of irradiation embrittlement effect on fatigue life of a pressurized-water reactor pressure vessel using the fracture toughness master curve approach

M.N. Tran [a,b,*], O. Muránsky [a,b], B.W. Spencer [c]

[a] Australian Nuclear Science and Technology Organisation (ANSTO), Lucas Heights, NSW 2234, Australia
[b] School of Mechanical and Manufacturing Engineering, University of New South Wales, Kensington, NSW 2052, Australia
[c] Computational Mechanics & Materials, Idaho National Laboratory, P.O. Box 1625, Idaho Falls, ID, USA

ARTICLE INFO

Keywords:
Irradiation embrittlement
Fracture toughness master curve
Fatigue life

ABSTRACT

The reactor pressure vessel (RPV) is a critical structural component in pressurized-water reactors, and it is designed to withstand extreme conditions, such as high pressures, elevated temperatures, and prolonged radiation exposure. Ensuring RPV integrity is essential for the safe and reliable long-term operation of nuclear power plants, especially as aging mechanisms such as fatigue and irradiation embrittlement pose increased risks. Fatigue, caused by cyclic thermal and mechanical loading, can lead to crack initiation in localized high-stress regions. Simultaneously, neutron irradiation, particularly in the beltline region, progressively reduces fracture toughness, increasing susceptibility to brittle fracture. These combined effects of fatigue and irradiation embrittlement potentially impact the RPV structural integrity, necessitating fitness-for-service assessments.

This study applies the fracture toughness master curve approach to evaluate the impact of irradiation embrittlement on RPV fatigue life. A coupled thermo-mechanical stress analysis identifies critical stress locations under normal service transients, pinpointing regions most vulnerable to fatigue crack initiation and growth. Stress intensity factors for postulated flaws at these locations are calculated, enabling an assessment of fatigue life under irradiated and unirradiated conditions. The results indicate that neutron irradiation embrittlement accelerates the conditions in which a critical crack can form and lead to failure, particularly at lower temperatures. The failure occurs where reduced fracture toughness limits the material's resistance to crack growth. Axial cracks at nozzle corners are the most life limiting without irradiation, while circumferential cracks demonstrate longer fatigue lives. The findings highlight the importance of incorporating irradiation effects into fatigue life predictions to ensure the long-term structural integrity of RPVs.

1. Introduction

The reactor pressure vessel (RPV) is one of the most critical and life-limiting structures of any nuclear reactor system. For pressurized-water reactor (PWR) applications, it is designed to withstand operating conditions that include a combination of elevated temperatures and high pressures while under material properties altering neutron flux. Hence, the integrity of the RPV is essential for the long-term safe and reliable operation of the plant. As modern reactors are designed to operate for 60 years or more (International Atomic Energy Agency, 2009a), ensuring the durability and structural integrity of the RPV has become paramount. Aging mechanisms such as fatigue and irradiation embrittlement are of critical concern, necessitating an evaluation of their combined effects in long-term operation of the nuclear reactor system.

Fatigue is a prevalent failure mode in nuclear reactor structures and can play a significant role in the aging process of RPVs. Fatigue arises from the progressive deterioration of material strength and structural integrity due to repeated cyclic loading, which results from fluctuating thermal and mechanical loads during plant operations. Over time, these cyclic stresses can lead to the initiation of cracks in areas of the RPV where the material experiences the greatest localized microstructural damage (Dowling, 2013). These critical regions are often associated with geometric discontinuities, stress concentrators, or areas exposed to harsh environmental conditions (International Atomic Energy Agency, 2023).

In addition to fatigue, the RPV shell materials, especially in the beltline region adjacent to the active fuel, are continuously exposed to

* Corresponding author at: Australian Nuclear Science and Technology Organisation (ANSTO), Lucas Heights, NSW 2234, Australia.
E-mail addresses: tranm@ansto.gov.au (M.N. Tran), omz@ansto.gov.au (O. Muránsky), benjamin.spencer@inl.gov (B.W. Spencer).

https://doi.org/10.1016/j.nucengdes.2025.114269
Received 6 February 2025; Received in revised form 27 May 2025; Accepted 23 June 2025
Available online 12 July 2025

Nomenclature

ART	Adjusted reference temperature (°C)
a	Crack depth (m)
a/c	Flaw aspect ratio
a_0	Initial crack depth (m)
a_0/c_0	Initial flaw aspect ratio
a_0/t	Initial through-wall crack depth ratio
a_e	Crack depth during a transient e (m)
a_f/t	Final through-wall crack depth ratio
a_i	Current total crack depth (m)
a_{i+1}	Next total crack depth (m)
C	Scaling constant for the Paris equation
C_{Ae}	Scaling constant for the Paris equation at the deepest point A during a transient e
C_{Be}	Scaling constant for the Paris equation at the surface point B during a transient e
CF	Chemistry factor, a function of copper and nickel content (°F)
Cu	Copper (weight %)
c	Half crack length (m)
c_0	Initial half crack length (m)
c_e	Half crack length during a transient e (m)
c_i	Current total half crack length (m)
c_{i+1}	Next total half crack length (m)
da/dN	Fatigue crack growth rate (m/cycle)
da_e/dN_e	Fatigue crack growth rate in the depth direction during a transient e (m/cycle)
dc_e/dN_e	Fatigue crack growth rate on the surface direction during a transient e (m/cycle)
d_e	Equivalent hydraulic diameter (m)
E	Number of transients
e	Normal operating transient event
FCG	Fatigue crack growth
f	Neutron fluence at any depth in the wall (10^{19}n/cm^2, E > 1 MeV)
f_{surf}	Neutron fluence at the inner wetted surface of the vessel at the location of the postulated defect (10^{19}n/cm^2, E > 1 MeV)
G	Mass flow rate (kg/m^2·s)
Gr_f	Free-convection Grashof number
g	Acceleration of gravity (m/s^2)
h	Heat-transfer coefficient (W/m^2·K)
iRT_{NDT}	Initial reference temperature of nil-ductility temperature (°C)
K_I	Stress intensity factor due to mode I fracture (MPa m$^{0.5}$)
$K_{IA,\max}$	Maximum stress intensity factor due to mode I fracture at the deepest point A (MPa m$^{0.5}$)
K_{IAe}	Stress intensity factor due to mode I fracture at the deepest point A during a transient e (MPa m$^{0.5}$)
$K_{IAe,\max}$	Maximum stress intensity factor due to mode I fracture at the deepest point A during a transient e (MPa m$^{0.5}$)
$K_{IAe,\min}$	Minimum stress intensity factor due to mode I fracture at the deepest point A during a transient e (MPa m$^{0.5}$)
$K_{IB,\max}$	Stress intensity factor due to mode I fracture at the surface point B (MPa m$^{0.5}$)
K_{IBe}	Stress intensity factor due to mode I fracture at the surface point B during a transient$e$(MPa m$^{0.5}$)
$K_{IBe,\max}$	Maximum stress intensity factor due to mode I fracture at the surface point B during a transient e (MPa m$^{0.5}$)
$K_{IBe,\min}$	Minimum stress intensity factor due to mode I fracture at the surface point B during a transient e (MPa m$^{0.5}$)
K_{Ic}	Fracture toughness (MPa m$^{0.5}$)
$K_{\max}$	Maximum stress intensity factor (MPa m$^{0.5}$)
$K_{\min}$	Minimum stress intensity factor (MPa m$^{0.5}$)
k	Thermal conductivity (W/m·K)
LEFM	Linear elastic fracture mechanics
M	Margin
$m(x,a)$	Weight function
N_e	Total number of cycles in a normal operating transient e (cycles)
Ni	Nickel (weight %)
Nu_f	Free-convection Nusselt number
Nu_d	Forced-convection Nusselt number
n	Slope of the $\log(da/dN)$ versus $\log(\Delta K_I)$ for the Paris equation
n_{Ae}	Slope of the $\log(da/dN)$ versus $\log(\Delta K_I)$ for the Paris equation at the deepest point A during a transient
n_{Be}	Slope of the $\log(da/dN)$ versus $\log(\Delta K_I)$ for the Paris equation at the surface point B during a transient
P	Phosphorus (weight %)
Pr_f	Free-convection Prandtl number
Pr_d	Forced-convection Prandtl number
PWR	Pressurized-water reactor
R	Stress ratio ($K_{\min}/K_{\max}$)
R_{Ae}	Stress ratio at the deepest point A during a transient
R_{Be}	Stress ratio at the surface point B during a transient
Re_d	Reynolds number
R_i	Inner radius (m)
RPV	Reactor pressure vessel
RT_{NDT}	Reference temperature of nil-ductility temperature (°C)
SIF	Stress intensity factor
$T(t')$	Time-dependent crack tip temperature (°C)
t	Thickness (m)
t'	Time
USE	Upper shelf energy
USE_c	Charpy V-notch upper shelf energy
USE_i	Irradiated upper shelf energy (ft-lb)
USE_u	Unirradiated upper shelf energy (ft-lb)
x	Through-wall distance from the inner surface moving positive toward the tip of the crack (m)
β	Temperature coefficient of volumetric expansion (K^{-1})
Δa	Cumulative crack depth increment after a time period (m)
Δa_e	Crack depth increment during a transient e (m)
Δc	Cumulative half crack length increment after a time period (m)
Δc_e	Half crack length increment during a transient e (m)
ΔK_I	Stress intensity factor range due to mode I fracture (MPa m$^{0.5}$)
ΔK_{IAe}	Stress intensity factor range due to mode I fracture at the deepest point A during a transient e (MPa m$^{0.5}$)
ΔK_{IBe}	Stress intensity factor range due to mode I fracture at the surface point B during a transient e (MPa m$^{0.5}$)
ΔK_{th}	Stress intensity factor range threshold (MPa m$^{0.5}$)
ΔK_{thAe}	Stress intensity factor range threshold at the deepest point A during a transient e (MPa m$^{0.5}$)
ΔN_e	Number of cycles during a transient e (cycles)
ΔRT_{NDT}	Shift in reference temperature of nil-ductility transition (°C)
ΔT	Temperature difference between the wall and the fluid

	(assumed to be 3 K)
μ	Dynamic viscosity (Pa·s)
ν	Kinematic viscosity (m^2/s)
$\sigma(x)$	Stress distribution along the crack plane (MPa)
$\sigma_{e,\max}$	Maximum stress distribution along the crack plane during a transient e (MPa)
$\sigma_{e,\min}$	Minimum stress distribution along the crack plane during a transient e (MPa)
$\sigma_{\max}$	Maximum stress distribution along the crack plane (MPa)
$\sigma_{\min}$	Minimum stress distribution along the crack plane (MPa)
σ_{ys}	0.2% offset yield strength at the upper shelf temperature (MPa)
$\Phi t'$	Neutron fluence is neutron flux (Φ) integrated over time (t') (neutron/cm^2)

high levels of neutron irradiation. This exposure degrades the material's mechanical properties over time through a process known as irradiation embrittlement. Specifically, prolonged neutron irradiation reduces the fracture toughness of RPV steels, making the material more prone to brittle fracture, particularly at lower operating temperatures. This embrittlement is characterized by changes in the material's microstructure, including the formation of matrix-feature defects such as vacancies and dislocation loops (International Atomic Energy Agency, 2009a), as well as precipitates (Eason et al., 2013); all of which hinder its ability to resist crack initiation and growth.

The combined effects of thermo-mechanical cyclic loading and neutron irradiation can have a significant impact on the fatigue life and overall structural integrity of RPVs. As a result, the effect of irradiation embrittlement on fatigue life should be considered in fitness-for-service assessments and in the development of long-term operation strategies for nuclear power plants. Traditional fatigue analyses, including cumulative usage factor method, omit irradiation embrittlement effects. This can underestimate the rates of crack growth and the reduction in fracture toughness, compromising safety during extended plant operation. A promising method for evaluating the effects of irradiation on RPV steels is the fracture toughness master curve (or K_{Ic} master curve) approach (International Atomic Energy Agency, 2009b; International Atomic Energy Agency, 2005a), which provides a systematic approach to assess fracture toughness over a range of temperatures. By applying the master curve approach, the extent of embrittlement and its impact on fatigue life can be predicted, enabling more reliable assessments of the long-term integrity of RPVs under irradiated conditions.

This paper presents an application of the K_{Ic} master curve approach to assess the effect of irradiation embrittlement on the fatigue life of a PWR RPV under Service Level A normal operating conditions. A design based on a two-loop Westinghouse PWR is utilized as a case study due to the availability of data (Westinghouse Electric Company, 2011). A coupled thermo-mechanical stress analysis of the RPV, considering typical normal service transients, was performed. Critical locations on the RPV were identified based on stress response, with particular attention to the beltline region. The stress intensity factors (SIFs) for postulated flaws were then calculated at these critical locations, followed by an evaluation of fracture responses and the reactor's fatigue life under irradiated and unirradiated conditions. By incorporating neutron irradiation effects into fatigue assessments, this study offers valuable insights into the long-term structural integrity of RPVs.

2. Methodology

2.1. Finite element model

A solid model of an RPV was constructed based on the dimensions outlined in Westinghouse's design control documents for the AP1000 reactor. These documents are openly accessible in the U.S. Nuclear Regulatory Commission Agencywide Documents Access and Management System (ADAMS) public repository (Westinghouse Electric Company, 2011). Fig. 1 shows the 3D solid model of the RPV, accompanied by a quarter cross-section to provide the inside view of the RPV. The RPV is approximately 12 m tall, with an inner diameter of roughly 4 m, and a wall thickness of about 220 mm. The model was developed using the

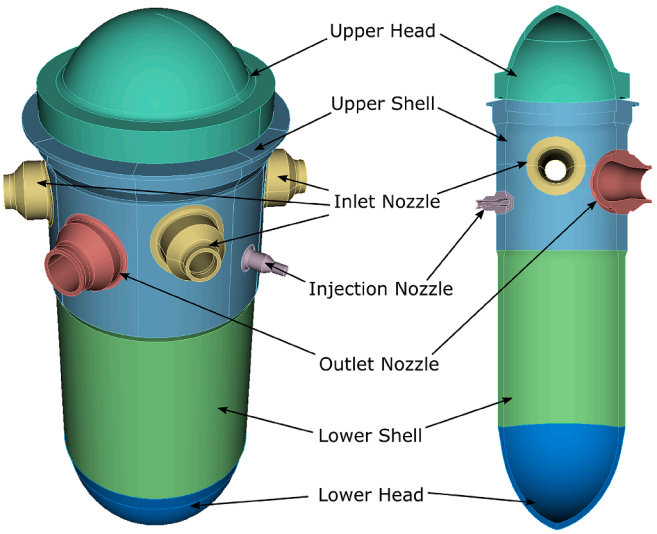

Fig. 1. Model of RPV, inlet, outlet, and injection nozzles.

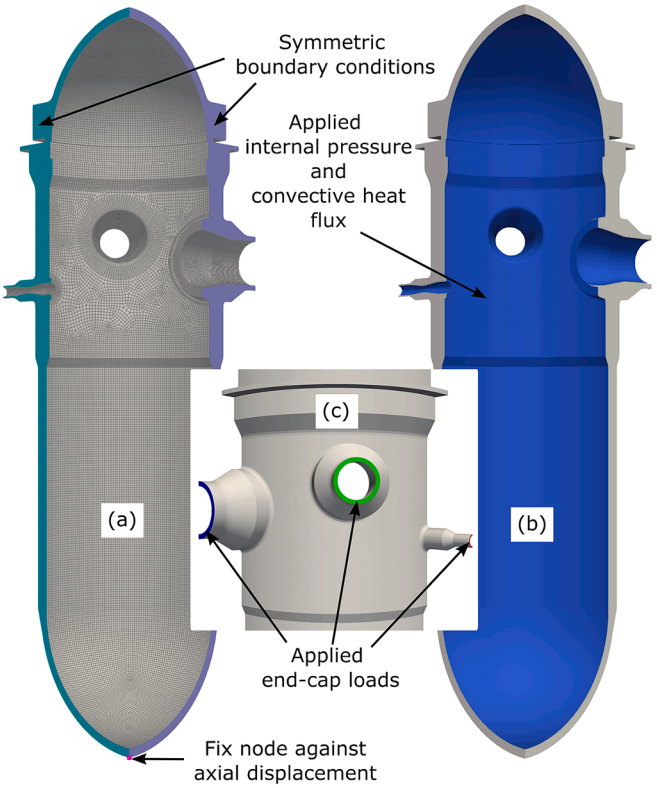

Fig. 2. (a) FE mesh of a quarter-symmetry 3D RPV showing symmetric boundary conditions, (b) applied internal pressure and convective heat flux, and (c) applied end-cap loads.

open-source FreeCAD software package (Riegel et al., 2011–2023). The model consists of the RPV shells and heads, four inlet nozzles, two outlet nozzles, and two injection nozzles.

The developed solid model was meshed using Coreform Cubit (Cubit, 2024), providing a finite element (FE) discretization for the RPV geometry. Fig. 2 shows a 3D quarter-symmetry meshed FE model of the RPV with 237,925 eight-node linear hexahedral elements. Symmetric boundary conditions were applied to represent the quarter-symmetry model, as illustrated in Fig. 2a. A node located at the base of the FE model was constrained against displacement in the axial direction.

Structural integrity assessments of reactor components involve solving coupled systems of partial differential equations. In this work, the BlackBear code (BlackBear Source Code Repository), built on the MOOSE (Multiphysics Object-Oriented Simulation Environment) framework (Lindsay et al., 2022), was employed to perform the thermal and mechanical stress analyses. For simplicity, the RPV and its nozzles were assumed to consist entirely of SA-508 steel base metal, with temperature-dependent material properties obtained from Reference (Muránsky et al., 2011).

It should be noted that flaws located in weld regions, particularly those joining RPV forgings in the beltline area, can significantly affect the structural integrity of the RPV under operating conditions. Weld flaws generally exhibit fatigue characteristics different from those of base metal, especially under neutron irradiation and thermo-mechanical cyclic loading. However, evaluating such weld flaws is outside the scope of this study.

2.2. Loading conditions

The design and construction of RPVs are typically evaluated according to the American Society of Mechanical Engineers (ASME) Boiler & Pressure Vessel Code Section III requirements for Class 1 components to ensure fitness for service. The evaluation process began with a system-level thermal–hydraulic analysis to generate the temperature and pressure histories experienced by the RPV during operation. These temperature and pressure histories were then applied to a thermo-mechanical model of the vessel. The resulting stress profiles at critical locations on the RPV were used as inputs for detailed fracture-mechanics assessments of individual flaws.

In this study, the fitness-for-service evaluation focuses on design conditions, serving as a representative example of the overall assessment process. The analysis primarily addresses the pressure and temperature loadings that form the basis for the design and are expected to occur during normal operating conditions. These normal conditions, categorized as Level A Service Conditions, require a detailed assessment of fatigue due to cyclic stresses. These stresses arise during system startup, operation in the design power range, hot standby, and system shutdown.

Table 1 presents an overview of the design transients, their corresponding descriptions, and the number of transients. This information is necessary for evaluating fatigue life under Level A Service Conditions (Westinghouse Electric Company, 2011). These design transients were used to derive the applied internal pressure, end-cap loads, and heat-transfer coefficients for the RPV and its inlet, outlet, and injection nozzles. The internal pressure and thermal loading were applied to the inner surface of the FE model as shown in Fig. 2b. The induced end-cap loads were applied to the free ends of the nozzles, illustrated in Fig. 2c, to account for the axial stress due to internal pressure.

The heat-transfer coefficient (or film coefficient) is a quantitative characteristic of convective heat transfer between a fluid (water) and the wall surface (inner surface of the RPV and its nozzles). There are two modes of convective heat transfer: natural (or free) convection and forced convection. Natural convection involves heat transfer driven solely by the fluid's inherent motion. In the case of forced convection, external forces actively influence the fluid's movement. Throughout reactor system operation, forced convection is the dominant mode of heat transfer. This is driven by external forces, such as coolant pumps,

Table 1
Service Level A design transients, descriptions, and number of cycles expected during normal operating condition.

Transient	Description	Cycles
1	Reactor coolant pump startup and shutdown (cycles of start and stop)	
1a	Cold startup transients	200
1b	Reactor coolant system heat-up and cool-down	200
1c	Hot functional reactor coolant pump stops and starts	400
1d	Transients and miscellaneous	2,200
2a	Heat-up at 100 °F/hr (55.6 °C/hr)	200
2b	Cool-down at 100 °F/hr (55.6 °C/hr)	200
3a	Unit loading between 0% and 15% full power (FP)	500
3b	Unit unloading between 15% and 0% FP	500
4a	Unit loading at 5%/min between 15% and 100% FP	2,000
4b	Unit unloading at 5%/min between 100% and 15% FP	2,000
5a	Step load increase of 10% FP between 15% and 100% FP	3,000
5b	Step load decrease of 10% FP between 100% and 15% FP	3,000
6	Large step load decrease with steam dump	200
7	Steady-state fluctuation and load regulation	
7ai	Initial	75,000
7aii	Initial	75,000
7bi	Random	2,300,000
7bii	Random	2,300,000
7c	Load regulation within 15% to 95% FP	750,000
8	Boron concentration equalization	2900
9	Feedwater cycling at hot shutdown	
9a	Mode 1 (every 2 hrs)	3,000
9b	Mode 2 (every 24 mins)	15,000
10	Core lifetime extension	40
11	Feedwater heaters out of service	180
12	Refueling	40
13	Turbine roll test	20
14	Primary-side leakage test	200
15	Secondary-side leakage test	80
16	Core makeup tank high-pressure injection test	5
17	Passive residual heat removal tests	5
18	Reactor coolant system makeup	2,820
19	Daily load follow operation	17,800

which propel the fluid's movement. When the reactor system is not active, natural convection takes precedence in the absence of external forces, allowing fluid motion to be guided purely by natural influences.

For natural convection in enclosed spaces, the internal heat-transfer coefficients can be calculated with (Holman, 2010):

$$Nu_f = 0.55\left(Gr_f Pr_f\right)^{1/4}$$

$$\frac{hd_e}{k} = 0.55\left[\left(\frac{g\beta\Delta T d_e^3}{\nu^2}\right)Pr_f\right]^{1/4} \tag{1}$$

where Nu_f, Gr_f, and Pr_f are the free-convection Nusselt, Grashof, and Prandtl numbers, respectively, h is the heat-transfer coefficient, d_e is the equivalent hydraulic diameter, k is the thermal conductivity of the fluid, g is the acceleration of gravity, β is the temperature coefficient of volumetric expansion, ΔT is the temperature difference between the wall and the fluid, and ν is the kinematic viscosity. For forced convection, when considering fully developed turbulent flow within smooth tubes for fluid heating, the corresponding internal heat-transfer coefficients are given by (Holman, 2010):

$$Nu_d = 0.023 {Re_d}^{0.8} Pr_d^{0.4}$$

$$\frac{hd_e}{k} = 0.023\left(\frac{Gd_e}{\mu}\right)^{0.8} Pr_d^{0.4} \tag{2}$$

where Nu_d, Re_d, and Pr_d are the forced-convection Nusselt, Reynolds, and Prandtl numbers, respectively, G is the mass flow rate, and μ is the dynamic viscosity.

The thermophysical properties of water, as functions of pressure and temperature, are readily accessible in References (Holman, 2010;

Rohsenow et al., 1998; Wagner and Kretzschmar, 2008), which provided the necessary parameters for Eqs. (1) and (2). The heat-transfer coefficients in Eqs. (1) and (2) can subsequently be calculated for natural and forced convections, respectively. These heat-transfer coefficients were then used to apply convective flux boundary conditions to the interior surfaces of the RPV and its nozzles as shown in Fig. 2b. Detailed pressure, temperature, and heat-transfer coefficients for inside the RPV and the inlet, outlet, and injection nozzles, calculated using the above equations, are provided for each transient in Appendix Table A1. Since reactor systems are typically well-insulated, it is reasonable to assume that no heat loss is occurring across the exterior surfaces of the RPV. This assumption is conservative, as it results in the maximum thermal gradient across the wall thickness. Furthermore, the heat-up and cool-down rates were maintained below 55 K/h (55 °C/hr or 100 °F/hr) for temperatures above the hot standby temperature of 450 K (175 °C) within the reactor system. The material's stress-free temperature was set at the ambient temperature of 294 K (21 °C).

2.3. Stress intensity factor calculation

After computing the stress field for the full RPV through the FE model, the subsequent analysis stage focuses on determining the SIFs using the weight function methodology. Guidance for calculating SIFs using the weight function method is outlined in the ASME Code, Section XI, Nonmandatory Appendix A, Article A-3000 (ASME, 2019). The weight function approach enables calculating SIFs for arbitrary surface-breaking cracks, using stress distributions acting normal to the crack plane. The weight function approach relies on the superposition principle, which was originally proposed by Bueckner (Bueckner, 1970) and subsequently elaborated on by Rice (Rice, 1972). The superposition principle demonstrates that the SIF on a crack face stemming from a load state, achieved through applied far-field surface tractions, is equivalent to the SIF arising from the application of tractions at the location of the crack due to the same load state if that crack was not present.

In this study, hypothetical 2D internal semi-elliptical surface-breaking cracks in both axial and circumferential directions were evaluated at a few critical locations inside the RPV. These locations are where the axial and hoop stresses are the greatest and were chosen because these stresses are primary drivers of circumferential and axial cracks, respectively. Additionally, a location in the beltline region, where irradiation embrittlement is most severe, was also considered. Fig. 3 illustrates these internal semi-elliptical surface-breaking cracks in a cylinder, with point A representing the deepest point and point B representing the surface point. The SIFs at these locations for mode I fracture, K_I, were calculated by integrating the product of the weight function, $m(x, a)$, provided by ASME Code Section XI, Article A-3000 (ASME, 2019), and the stress distribution, $\sigma(x)$, along the crack plane extracted from the FE model, expressed as:

$$K_I(a) = \int_0^a m(x,a)\,\sigma(x)dx \tag{3}$$

where x is the through-wall distance from the inner surface moving positive toward the tip of the crack and a is the crack depth. A range of initial crack depths, a_0, was considered, varying from 5% to 80%[1] of the wall thickness with increments of 0.1%. The initial half crack length, c_0, was assumed to be three times the initial crack depth, consistent with the guidelines provided in ASME Code Section XI, Appendix L (ASME, 2019). The flaw aspect ratio, a/c, was allowed to vary throughout the calculation of the SIFs as the crack evolves.

Fracture toughness, K_{Ic}, is a material property representing the critical SIF value, above which a crack may experience unstable propagation, potentially resulting in sudden failure. The K_{Ic} value used in this study is based on the lower bound of static-initiation K_I values, which are a function of time-dependent temperature, $T(t')$, and reference nil-ductility temperature, RT_{NDT}. Although stable crack growth can occur within the brittle-to-ductile transition region, where it is more appropriately characterized by a J-R curve, the conservative approach adopted here ensures that the SIFs remain below K_{Ic}. The specific K_{Ic} values utilized were obtained from ASME Code Section XI, Article A-4200 (ASME, 2019), as follows:

$$K_{Ic}(T(t') - RT_{NDT}) = 36.5 + 22.783\exp[0.036(T(t') - RT_{NDT})]. \tag{4}$$

2.4. Irradiation embrittlement

Irradiation embrittlement is a significant concern for reactor components, as it can lead to premature failure under the high pressures and temperatures encountered during operation or increase the likelihood of failure under off-normal conditions. It is a key factor in the design, maintenance, and life extension of nuclear reactors. The beltline region of the RPV, located adjacent to the reactor core, is particularly susceptible to irradiation embrittlement due to its exposure to high neutron fluence (ASTM E185, 1998). This elevated neutron exposure can increase the ductile-to-brittle transition temperature, reducing the fracture toughness and ductility of RPV steels (Odette and Lucas, 2001).

The master curve approach offers a robust method to assess the effects of irradiation embrittlement by characterizing the fracture toughness of RPV steels as a function of temperature, based on RT_{NDT}. By employing the master curve in conjunction with a model for the irradiation-induced shift in RT_{NDT}, the reduction in fracture toughness due to neutron irradiation can be quantified. The master curve with the shifted RT_{NDT} quantifies the material's transition from ductile to brittle behavior at lower temperatures.

In the case of the AP1000 reactor, the RPV shell is constructed from SA-508 Grade 3 Class 1 steel (Westinghouse Electric Company, 2011). The master curve for this material, corresponding to an RT_{NDT} of 0 °C in Eq. (4), is represented by the solid black curve in Fig. 4a. To account for irradiation effects, the adjusted reference temperature (ART) of nil-ductility temperature (NDT) was calculated using the methodology outlined in the U.S. Nuclear Regulatory Commission's *Regulatory Guide 1.99*, Rev. 2 (US Nuclear Regulatory Commission, 1988), as follows:

$$ART = \mathrm{i}RT_{NDT} + M + \Delta RT_{NDT} \tag{5}$$

where the mean value of the adjustment in reference temperature caused by irradiation, ΔRT_{NDT} (in °F), was calculated as follows (US Nuclear Regulatory Commission, 1988):

$$\Delta RT_{NDT} = (CF)f^{(0.28-0.10\log f)}. \tag{6}$$

Based on the copper and nickel content for the base metal listed in Table 2 and the correlations in Reference (US Nuclear Regulatory Commission, 1988), the chemistry factor, CF, was determined to be 37.

Due to the relatively high scattering cross-section of steel for fast neutrons (typically E > 1 MeV), the fast neutron fluence diminishes as it penetrates through the RPV wall. The attenuation of neutron fluence, f, from the surface neutron fluence, f_{surf}, at any depth, x (in inches), into the vessel wall can be described by the following equation (US Nuclear Regulatory Commission, 1988):

$$f = f_{\mathrm{surf}}\exp(-0.24x). \tag{7}$$

Eq. (7) indicates that the neutron fluence is highest at the inner wetted surface, where the material is directly exposed to the neutron source. As neutrons penetrate deeper into the material, their fluence decreases exponentially. This attenuation occurs because the neutrons are absorbed by the material, losing intensity as they travel through it. Therefore, for semi-elliptical surface-breaking cracks, the surface point B (see Fig. 3) at the wetted surface experiences higher neutron fluence, leading

[1] Note that an 80% through-wall crack corresponds to the upper validity limit for the weight function method.

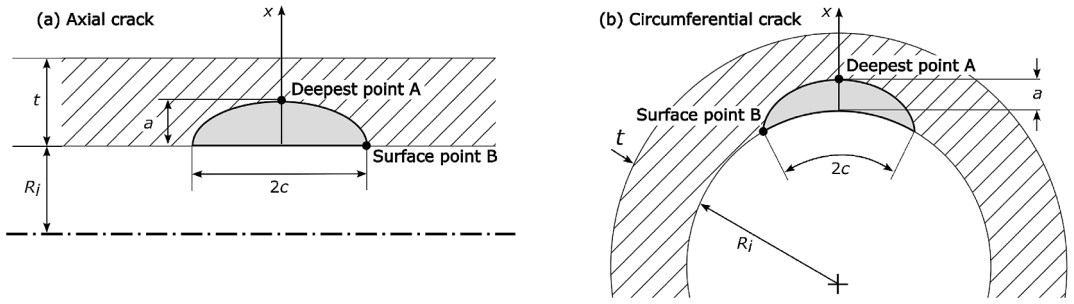

Fig. 3. Illustration showing internal semi-elliptical surface-breaking cracks in a cylinder: (a) axial crack and (b) circumferential crack.

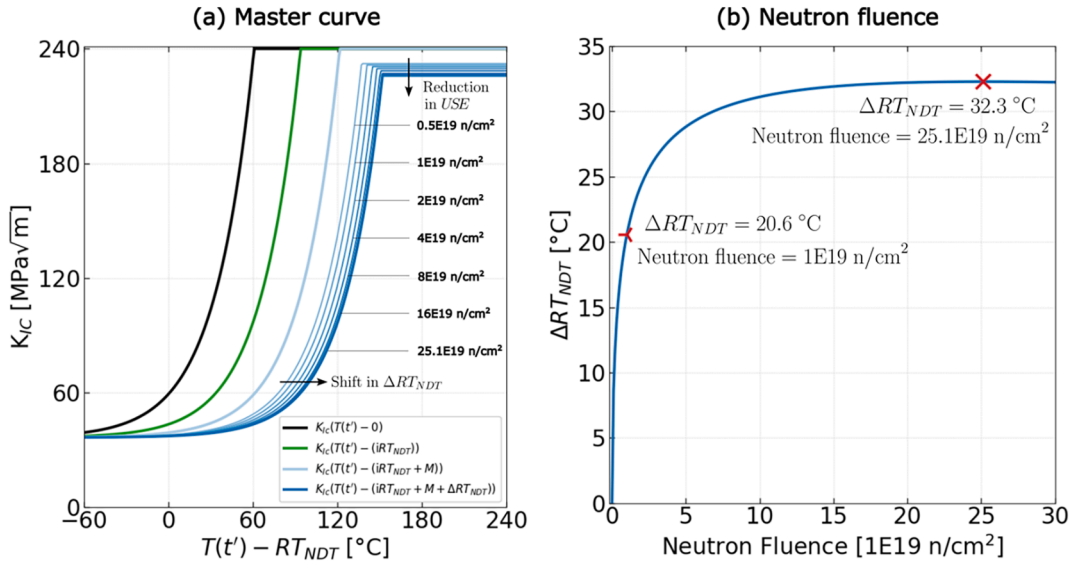

Fig. 4. (a) Effect of irradiation embrittlement on fracture toughness master curve and (b) variation of nil-ductility transition reference temperature, ΔRT_{NDT}, with neutron fluence following U.S. Nuclear Regulatory Commission Regulatory Guide 1.99, Rev. 2 (US Nuclear Regulatory Commission, 1988).

Table 2
Maximum limits for chemical elements of the AP1000 RPV (weight %).

	Copper	Phosphorus	Vanadium	Sulfur	Nickel
SA-508 Grade 3 Class 1	0.06	0.01	0.05	0.01	0.85

to higher irradiation-induced embrittlement. In contrast, the deepest point A (see Fig. 3) in the vessel wall is shielded by the surrounding material, resulting in lower neutron fluence and a slower rate of embrittlement.

A margin, *M*, of 27.78 °C (50 °F) was assumed for base metal (Choi et al., 2019), providing an upper bound for the *ART*. This margin accounts for uncertainties in both the initial nil-ductility reference temperature, iRT_{NDT}, and the shift in the nil-ductility transition reference temperature, ΔRT_{NDT}. The iRT_{NDT} was set at 33 °C (60 °F) as stipulated in Reference (US Nuclear Regulatory Commission, 2007). The *ART* was then substituted back into Eq. (4) in place of RT_{NDT} to calculate the master curve with irradiation embrittlement considered. The solid green curve in Fig. 4a illustrates the shift in the master curve due to the iRT_{NDT}, while the solid light-blue curve depicts the additional shift in the master curve resulting from both iRT_{NDT} and *M*.

Neutron fluence generally increases embrittlement in SA-508 Grade 3 Class 1 steel by promoting nano-precipitation (e.g., Cu, Ni, Mn, Si) and the formation of irradiation-induced matrix defects (Bai et al., 2017; International Atomic Energy Agency, 2005b; Jiang, 2024; Odette, 1994). Once the solubility limit of these precipitating elements is reached, further precipitation does not significantly increase embrittlement (Bai et al., 2017; Ortner et al., 2024). However, it is essential to account for flux effects when comparing neutron fluence in typical power reactors with that in accelerated test reactors. High-flux conditions in accelerated tests often accelerate precipitation kinetics, whereas lower flux conditions typical of power reactor operation over 40 to 60 years may delay precipitation, potentially affecting predictions of embrittlement (Ortner et al., 2024).

In this study, SA-508 steel was assumed to contain the maximum chemical limits listed in Table 2 (Westinghouse Electric Company, 2011). Under these conditions, Eq. (6) indicates that ΔRT_{NDT} reaches a maximum of about 32.3 °C at a neutron fluence of 25.1E19 n/cm^2, as marked in Fig. 4b. Although stable matrix defects can continue to form and incrementally harden the steel beyond this fluence, their effect on ΔRT_{NDT} is relatively small once the solubility-driven precipitate saturation is attained. As shown in Reference (Spencer et al., 2020), a typical 40-year reactor operation might accumulate a fluence of approximately 1E19 n/cm^2, assuming an annual fluence rate of 2.5E17 n/cm^2. At this neutron fluence level, ΔRT_{NDT} is around 20.6 °C, as depicted by the marker in Fig. 4b. The solid blue curve in Fig. 4a illustrates the shift in master curve resulting from the *ART* at the maximum ΔRT_{NDT} of 32.3 °C, corresponding to 25.1E19 n/cm^2 neutron fluence. The thin blue lines represent the master curve at various intermediate neutron fluence levels.

Although fracture toughness and Charpy V-notch tests measure different properties—fracture toughness tests quantify a material's resistance to the propagation of an existing crack, while the Charpy V-notch test measures the energy absorbed by a material during rapid

fracture under an impact load—they can be related at the upper shelf energy (*USE*). The *USE* corresponds to the energy absorbed by the material in the ductile zone (International Atomic Energy Agency, 2009a). At this upper shelf, the effects of loading rates and notch acuity are less critical compared to those in the transition-temperature region (Barsom and Rolfe, 1999). As a result, fracture toughness (K_{Ic}) can be estimated from Charpy V-notch upper shelf energy (USE_c). An empirical correlation between K_{Ic} and USE_c is provided in References (Barsom and Rolfe, 1999; Terán et al., 2016) as follows:

$$\left(\frac{K_{Ic}}{\sigma_{ys}}\right)^2 = 0.64\left(\frac{USE_c}{\sigma_{ys}} - 0.01\right) \tag{8}$$

where σ_{ys} is the 0.2% offset yield strength at the upper shelf temperature. From ASME Code Section XI, Nonmandatory Appendix A, Article A-4000 (ASME, 2019), the upper bound on K_{Ic} at *USE* was assumed to be 240 MPa $m^{0.5}$. Using this value, the USE_c can be calculated from Eq. (8). At the *USE*, RPV steels exhibit greater toughness due to their high ductility at elevated temperature, making them less prone to brittle fracture. The relationship between the unirradiated (USE_u, in ft-lb) and the irradiated (USE_i, in ft-lb) Charpy USE can be expressed through the following (Eason et al., 1998):

$$USE_i = 0.0570USE_u^{1.456} + \left\{\begin{array}{ll} 55.4, & \text{for welds} \\ 61.0, & \text{for plates} \\ 66.3, & \text{for forgings} \end{array}\right\}$$

$$-\left[17.5f(Cu)\left(1+1.17Ni^{0.8894}\right)+305P\right]\left(\frac{\Phi t'}{10^{19}}\right)^{0.2223} \tag{9}$$

where *Cu*, *Ni*, and *P* are the weight % of copper, nickel, and phosphorus, Φ is the neutron flux, and t' is the irradiation time, and

$$f(Cu) = \left[\frac{1}{2}+\frac{1}{2}\tanh\left(\frac{Cu-0.138}{0.0846}\right)\right]. \tag{10}$$

At the beginning of the RPV's service life, the USE_u was assumed to be equal to the USE_c. As the RPV is exposed to neutron irradiation, the USE_i decreases. This reduction in energy-absorbing capacity is described by Eqs. (9) and (10), which account for the effects of neutron fluence, the manufacturing process, and the material's composition, particularly the influence of copper, nickel, and phosphorus content. In this study, the value specific to the forging manufacturing process was used. The USE_i was then substituted back into Eq. (8) in place of USE_c to calculate the corresponding reduction in K_{Ic} in the ductile regime. The reduction in K_{Ic} at varying levels of neutron fluence is shown in Fig. 4a, illustrating the effect irradiation has on the material's ability to absorb energy.

2.5. Fatigue crack growth

For a given material, the crack growth behavior can be obtained through the relationship between the cyclic crack growth rate, da/dN, and the SIF range, $\Delta K_I = K_{max} - K_{min}$. The fatigue crack growth (FCG) rate for a material can be divided into three regimes: low growth, midrange growth, and high growth rates. Test data and corresponding fitted curves are generally presented on a log–log plot. At midrange growth rates, the fitted curve often forms a straight line. This linear relationship can be described by the Paris equation (Paris and Erdogan, 1963):

$$\frac{da}{dN} = C(\Delta K_I)^n \tag{11}$$

where *C* and *n* are a scaling constant and an exponent, respectively.

Fatigue crack growth behavior is influenced by the stress ratio, *R*, where higher values of *R* lead to an accelerated rate of crack growth. Conversely, when the ΔK_I falls below the threshold ΔK_{th}, the FCG rate becomes negligible, indicating that crack growth is effectively arrested under such conditions. The threshold SIF ranges, ΔK_{th}, as stipulated by ASME Code Section XI, are as follows:

$$\Delta K_{th} = 5.5 \text{ for } R < 0,$$

$$\Delta K_{th} = 5.5\,(1 - 0.8R) \text{ for } 0 \le R < 1.0. \tag{12}$$

For the SA-508 ferritic steel material exposed to a light-water reactor environment, the FCG rate follows the Paris Eq. (11), with parameters *C* and *n* specified in ASME Code Section XI, Article A-4000 (ASME, 2019). These parameters, and thus the FCG rate in the Paris equation, are not changed by irradiation.

In this study, the fatigue life, under thermo-mechanical cyclic loading, was evaluated using linear elastic fracture mechanics (LEFM). The process began with the calculation of maximum and minimum SIF values, K_{IAe}, at the deepest point *A*, and K_{IBe} at the surface point *B*, for each transient, *e*. Next, the maximum SIF values, $K_{IAe,\,max}$ and $K_{IBe,\,max}$, were compared to the fracture toughness value, K_{Ic}, at which failure was assumed to occur. If the failure condition was reached, the analysis was terminated. The SIF ranges, ΔK_I, at the deepest point *A* and surface point *B* for each transient were also evaluated. If they fell below the threshold value, ΔK_{th}, the crack ceased to propagate, and the analysis was terminated with no further crack growth. To account for crack growth over multiple transients, the superposition principle was utilized. The accumulated crack increments, Δa and Δc, over a given time period (1 year in this study) were determined by summing the contributions from each transient, Δa_e and Δc_e. The final crack size was calculated as the sum of the initial crack size and the total crack growth increment from all transients, *E*. A flowchart of this fatigue life evaluation procedure is provided in Fig. 5, detailing the process of tracking the crack evolution for both axially and circumferentially oriented cracks, starting from the initial crack size through to the final critical crack size.

3. Results and discussion

3.1. Stress analysis

The thermo-mechanical stress analysis was performed for all Service Level A design transients listed in Table 1, except for Transient 15 (secondary-side leakage test), which pertains to the secondary loop and is outside the scope of this analysis. Detailed pressure and temperature loadings, along with heat-transfer coefficients for each timestep, are provided in Table A1. The analysis identified the maximum axial and hoop stresses for each transient, the times at which they occurred, and their corresponding locations (referred to as critical locations) in the RPV. Fig. 6a identifies two critical locations at the surface wall: Critical Location 1 (CL1), corresponding to the maximum axial stress, and Critical Location 2 (CL2), corresponding to the maximum hoop stress.[2] Both these critical locations are situated on the upper shell of the RPV, at the inner corners of the inlet and outlet nozzles, where geometric and loading conditions promote high axial and hoop stresses. In addition, Fig. 6a introduces a third critical location, CL3, located in the middle of the RPV's lower inner shell wall in the beltline region. CL3 is considered critical not due to high operational stresses but because of the high neutron flux in this area, which leads to irradiation embrittlement of the RPV steel (SA-508 Class 1) (Spencer et al., 2020). A flaw in this irradiation-embrittled region could potentially become life limiting for the RPV, even when this region experiences lower stress levels compared to stresses in the other two critical locations (CL1 and CL2).

The progression of FCG is primarily influenced by $\Delta\sigma = \sigma_{max} - \sigma_{min}$, making it essential to identify the maximum and minimum stresses at the critical locations, as well as the timesteps at which they occur. The

[2] Note that the axial stresses resulting from the reactor operational transients promote the initiation and growth of circumferential cracks, while the hoop stresses promote the initiation and growth of axial cracks through the RVP wall thickness.

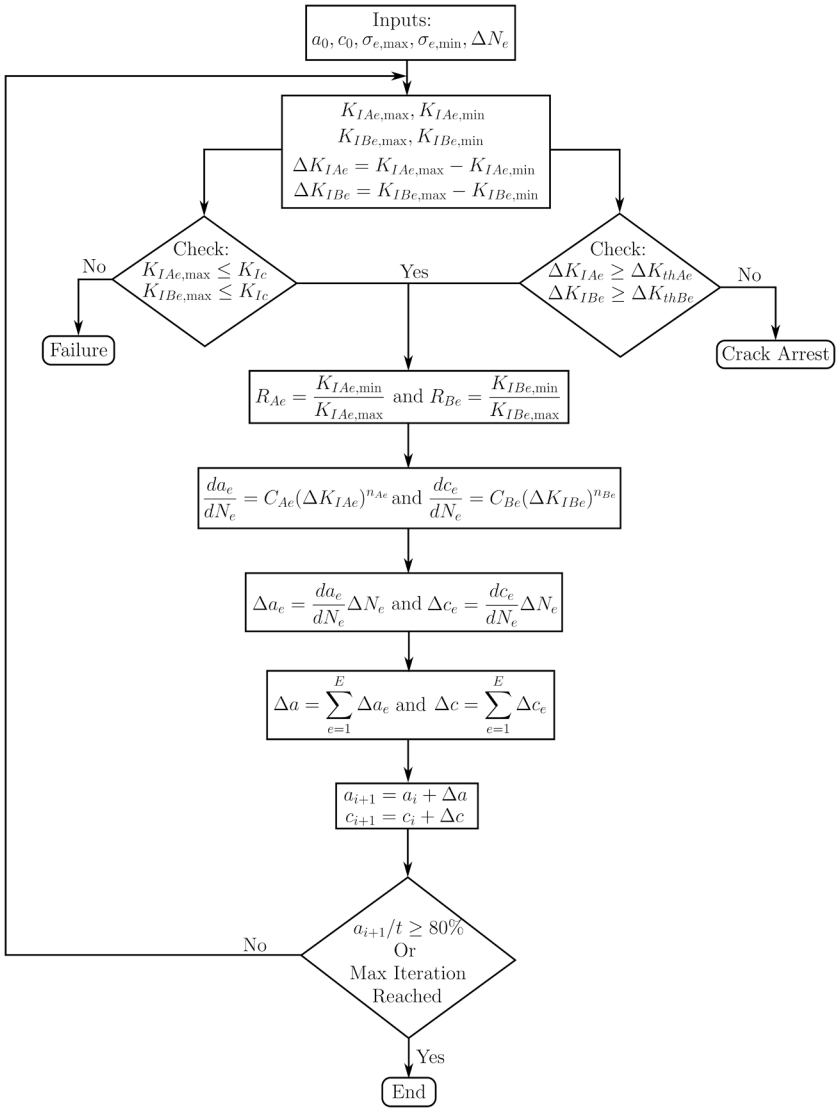

Fig. 5. Flowchart of FCG history calculation for all transients.

SIF range ΔK_I, which is proportional to $\Delta\sigma$ in LEFM analysis, drives FCG behavior. To illustrate the identification of these key timesteps, the two most severe transients are examined in detail: (a) Transient 2 (heat-up and cool-down), and (b) Transient 14 (primary-side leakage test); see Table A1. Transient 2 is the most stress-inducing among all analyzed transients; however, the high stresses occur at elevated temperatures, where the material exhibits greater ductility and is less prone to fracture. Transient 14 is less stress-inducing overall; however, this transient generates high stresses at low temperatures, making the material more brittle and susceptible to fracture. Fig. 7 illustrates the pressure and thermal loads associated with Transients 2 and 14, highlighting the critical timesteps where stress extremes occur. For Transient 2, Fig. 7a reveals that timestep T1 corresponds to the minimum axial and hoop stresses at all three critical locations. Timestep T2 is when the axial and hoop stresses at CL3 reach their maximum values, and timestep T3 is when the maximum axial stress at CL1 and the maximum hoop stress at CL2 are observed. For Transient 14, Fig. 7b indicates that timestep T1 corresponds to the minimum axial and hoop stresses at all three critical locations. At timestep T2, the maximum axial stress occurs at CL1. And at timestep T3, the maximum axial and hoop stresses occur at CL3, along with the peak hoop stress at CL2.

Fig. 6b and c provide cross-sectional views of the stress fields at stress extremes for Transients 2 and 14, respectively. These figures also highlight the critical path (indicated by a magenta arrow), representing the shortest through-wall distance where stress profiles were extracted for the follow-up SIF analysis (Section 3.2). Fig. 8 shows the through-wall stresses extracted along the critical paths at the three identified critical locations. For Transient 2, Fig. 8a and b shows that axial and hoop stress are the highest at the inner surface and rapidly decrease through the wall thickness at CL1 and CL2. A similar behavior can be observed for the hoop stresses at CL2 in Transient 14; however, the axial stress range at CL1 during this transient is lower at the inner surface and increases toward the outer surface. This increase is attributed to a slight concentration of stress at the outer upper corner of the outlet nozzle, caused by a combination of pressure loads and nozzle geometry. Fig. 8c and d show that axial and hoop stress ranges at CL3 for both Transients 2 and 14 remain relatively constant due to the uniform cylindrical geometry of the lower shell. Moreover, the hoop stress ranges at CL3 are about twice those of the axial stress ranges. The differences in stress ranges at the three critical locations suggest distinct SIF patterns, which are discussed in Section 3.2. Understanding these localized stress distributions is crucial for evaluating FCG behavior under Service Level A operating conditions.

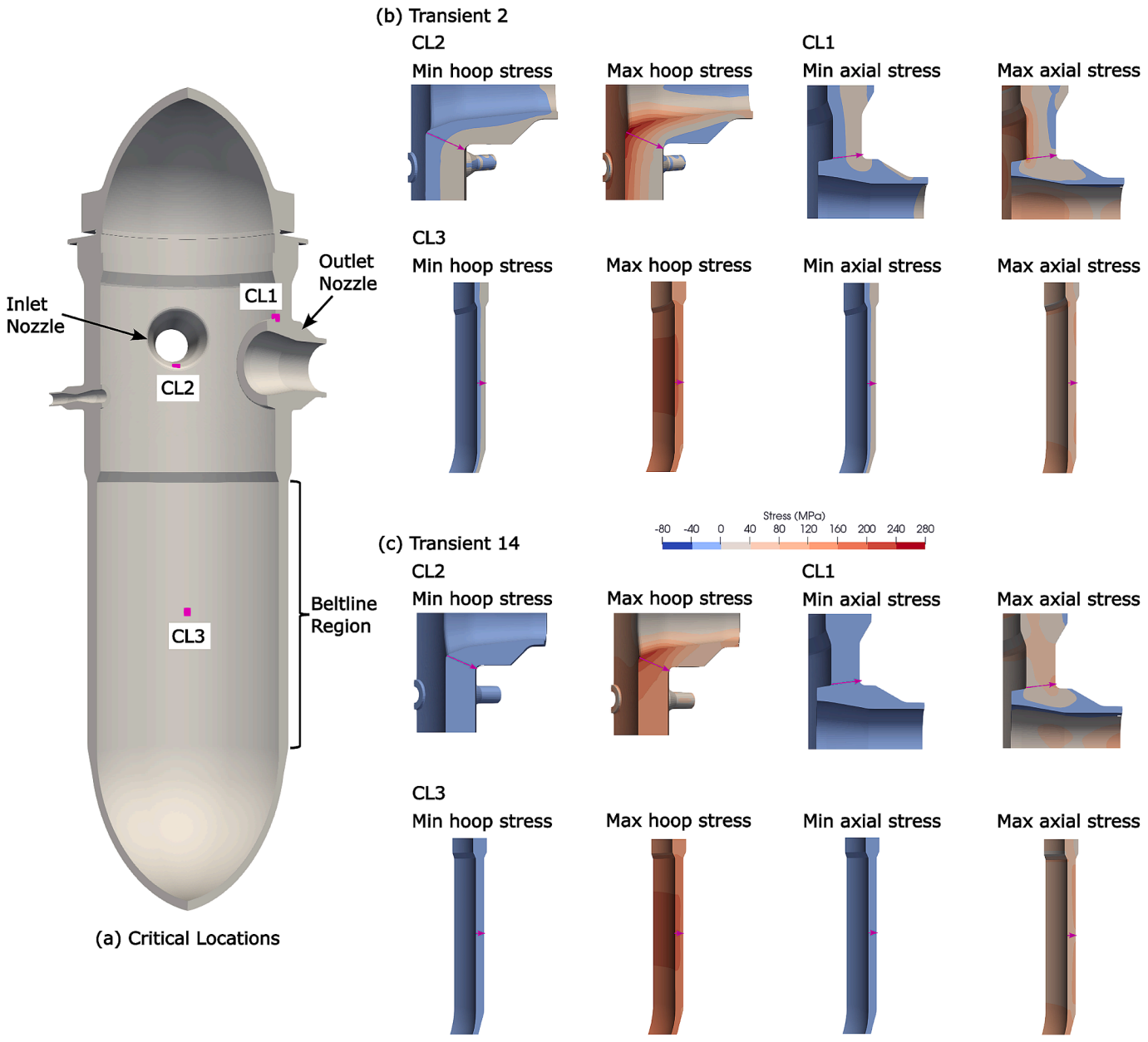

Fig. 6. (a) Critical locations on RPV with maximum and minimum axial and hoop stress fields for (b) Transient 2 (heat-up and cool-down) and (c) Transient 14 (primary-side leakage test).

3.2. Stress intensity factor analysis

To perform fatigue life analysis using LEFM, it is necessary to calculate the SIF range (ΔK_I) from the maximum and minimum K_I values. These K_I values[3] were computed by integrating the product of the weight function (Section 2.3) and the through-wall stress profiles (Fig. 8), which were extracted from the maximum and minimum stress extremes[4] observed during the most severe operating transients identified by the stress analysis as Transients 2 and 14 (Section 3.1). The K_I values were determined for crack depth to wall thickness ratios, a_0/t ranging from 0.05 to 0.8, while the initial aspect ratio of crack depth (a_0) to half crack length (c_0) was kept constant at $a_0/c_0 = 1/3$. These K_I values were calculated incrementally as the crack propagated until it reached a critical size, where K_I equaled the material's fracture toughness (K_{IC}), indicating critical crack growth leading to failure. The FCG calculation process is summarized in the flowchart shown in Fig. 5.

Fig. 9 illustrates the evolutions of maximum K_I values for both axial and circumferential cracks at the deepest point A and the surface point B (Fig. 3), from crack initiation (open symbols) to final crack depths at the three critical locations: CL1, CL2, and CL3. These results are presented for an initial crack depth of 5% through the vessel wall. Two K_{IC} master curves are shown: the solid green curve represents the fracture toughness of the as-received SA-508 steel (without considering the impact of irradiation embrittlement on its fracture toughness), and the solid blue curve accounts for neutron-irradiated SA-508 steel with a neutron fluence of 25.1E19 n/cm^2 (Section 2.4). While irradiation embrittlement

[3] Note that these K_I values were computed assuming cylindrical geometry. More sophisticated methods may yield different K_I values.

[4] Note that K_I values were calculated at each timestep in a transient for crack depth ratios a/t ranging from 5% to 80% of the wall thickness, in increments of 5%, at a constant $a/c = 1/3$. These K_I values were then summed from $a/t = 5\%$ to 80%. In each transient, the maximum stress profile corresponds to the highest K_I value and the minimum stress profile corresponds to lowest K_I value.

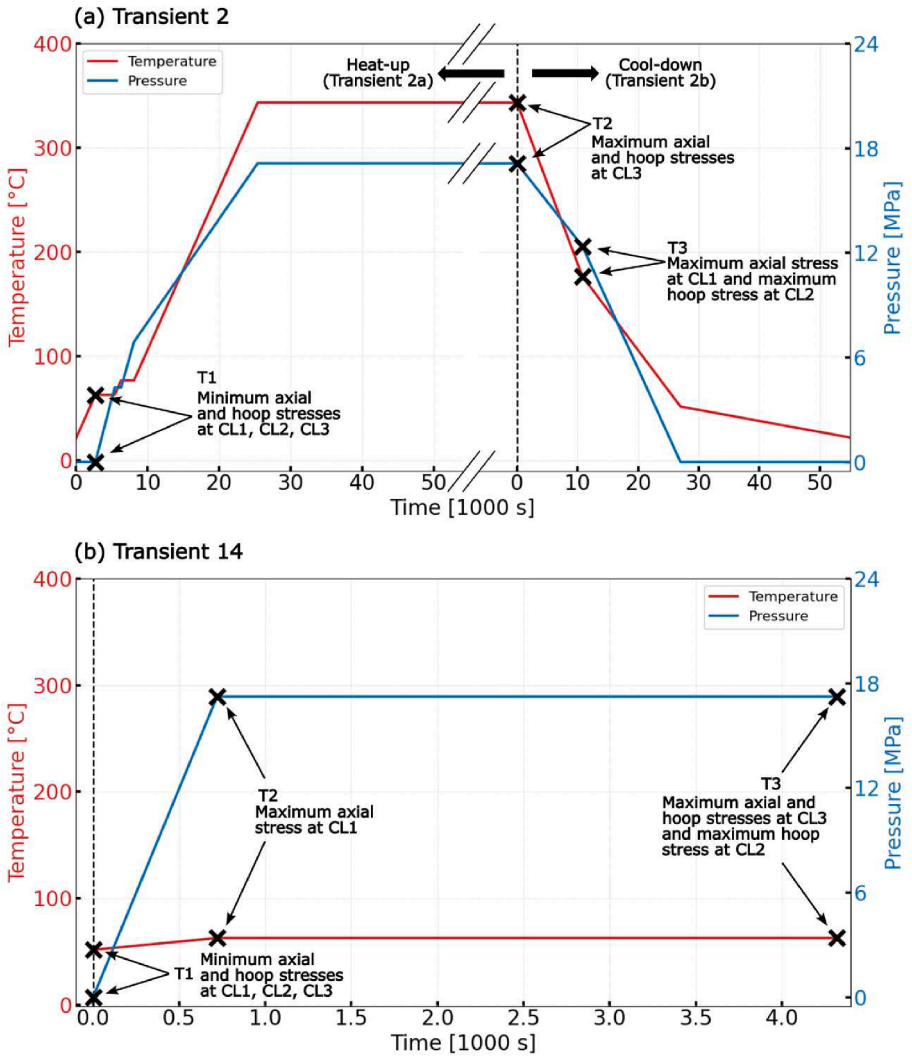

Fig. 7. Coolant pressure and temperature histories during (a) Transient 2 (heat-up and cool-down) and (b) Transient 14 (primary-side leakage test).

was not considered for the outlet and inlet nozzles (CL1 and CL2, respectively), as these locations are far from the reactor core (Fig. 6a), its impact was assessed in the beltline region at CL3 due to its proximity to high neutron fluence levels. To assess the impact of material embrittlement on FCG and ultimately the life of the RPV, analyses were performed both with and without considering irradiation embrittlement of the material.

The evolutions of maximum K_I values for axial cracks at the deepest point A and the surface point B are illustrated in Fig. 9a and 9b, respectively, under Transients 2 and 14. Reference (Tran et al., 2024) identified these two transients as having the highest FCG rates, underscoring their importance in evaluating crack growth behavior. When considering axial cracks, the hoop stresses at CL2 and CL3 are considered relevant. At CL2 during Transient 14 (Fig. 9a), the maximum K_I at the deepest point A, $K_{IA,\max}$, begins at approximately 53 MPa $m^{0.5}$ and grows to about 98 MPa $m^{0.5}$, intersecting the K_{IC} master curve (solid green curve) and indicating critical crack size. At CL3, both with and without irradiation embrittlement consideration, the initial $K_{IA,\max}$ value starts at around 28 MPa $m^{0.5}$ due to lower operational stresses (Fig. 8b and d). Without irradiation, $K_{IA,\max}$ increases to about 95 MPa $m^{0.5}$ when it intersects the K_{IC} master curve (solid green curve). When irradiation embrittlement is considered, $K_{IA,\max}$ intersects the K_{IC} master curve at a maximum neutron fluence of 25.1E19 n/cm^2 (solid blue curve) at 44 MPa $m^{0.5}$. This highlights a significant reduction in fracture toughness caused by irradiation-induced material embrittlement. The intersection of $K_{IA,\max}$ with the K_{IC} master curve at the maximum neutron fluence suggests that shallow initial cracks, which propagate over extended periods, experience higher neutron fluence levels. During Transient 2, the $K_{IA,\max}$ values at CL2 and CL3 are similar to those observed during Transient 14. However, higher crack tip temperatures during Transient 2 result in increased fracture toughness, preventing failure despite more severe hoop stresses, as shown in Fig. 8b.

At the surface point B in Fig. 9b, $K_{IB,\max}$ at CL2 for Transient 14 starts at approximately 35 MPa $m^{0.5}$ and grows to about 96 MPa $m^{0.5}$. At CL3, $K_{IB,\max}$ begins at about 19 MPa $m^{0.5}$, reaching 42 MPa $m^{0.5}$ with irradiation embrittlement and 97 MPa $m^{0.5}$ without it. Similar trends are observed for Transient 2, where higher temperatures increase fracture toughness. However, $K_{IB,\max}$ at CL2 and CL3 for both Transients 2 and 14 do not reach the fracture toughness threshold. Consequently, failure is more likely at the deepest points A, with or without irradiation embrittlement, for both locations and transients.

Fig. 9c and d examine circumferential cracks (Fig. 3b) at CL1 and CL3. When analyzing circumferential cracks, only CL1 and CL3 are considered, as the axial stresses in CL2 are not critical for driving circumferential crack growth to failure. At CL1 in Fig. 9c, $K_{IA,\max}$ for Transient 14 starts at approximately 10 MPa $m^{0.5}$ and increases to 71 MPa $m^{0.5}$ but does not intersect the K_{IC} master curve. For Transient 2, $K_{IA,\max}$ begins at about 44 MPa $m^{0.5}$ and increases to 96 MPa $m^{0.5}$. This increase is attributed to the thermal conditions during Transient 2 at CL1. Because CL1 is located at the upper corner of the outlet nozzle in

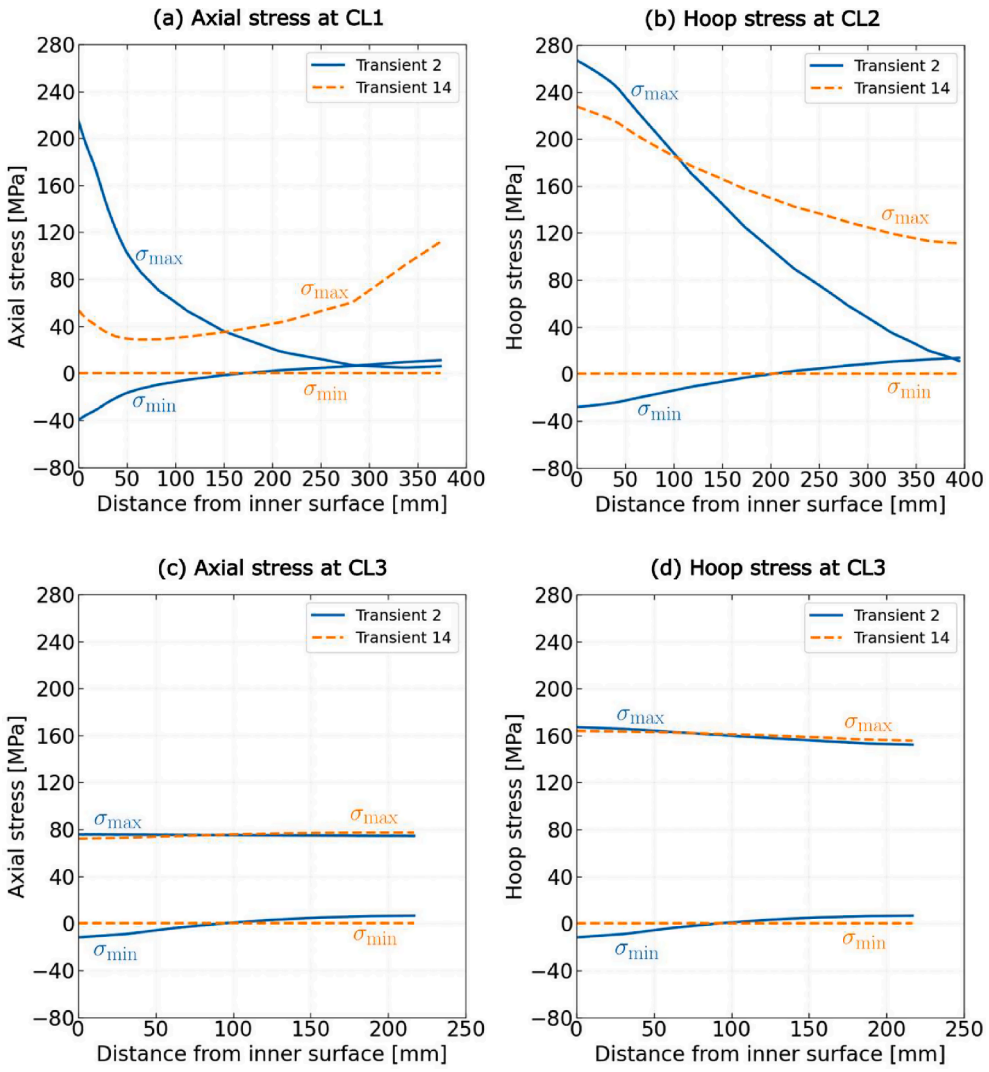

Fig. 8. Maximum and minimum axial and hoop stress profiles along critical paths for Transient 2 (heat-up and cool-down) and Transient 14 (primary-side leakage test).

the upper shell of the RPV (Fig. 6a), during the cool-down from operation in Transient 2[5] (Fig. 7a), the fully insulated RPV cools more slowly near the outer surface than near the inner surface. Hence, as the crack propagates outward from the inner surface, the crack tip moves into regions of higher temperature, leading to an increase in crack tip temperature as the crack grows. As a result of this temperature increase, $K_{IA,\max}$ at CL1 for both Transients 2 and 14 does not reach the fracture toughness threshold. Therefore, failure at the deepest points is unlikely at CL1.

At CL3 in Fig. 9c, $K_{IA,\max}$ begins at about 12 MPa $m^{0.5}$ for both irradiated and unirradiated conditions. Without irradiation embrittlement, $K_{IA,\max}$ grows to 91 MPa $m^{0.5}$ but does not reach the K_{IC} master curve. When irradiation embrittlement is considered, $K_{IA,\max}$ intersects the K_{IC} master curve (solid blue curve) at 43 MPa $m^{0.5}$, indicating potential failure due to reduced fracture toughness. For Transient 2, the $K_{IA,\max}$ values are comparable to those in Transient 14 but do not reach the K_{IC} master curve, meaning failure at CL3 occurs only under irradiation embrittlement during Transient 14.

Fig. 9d shows the K_I evolution for circumferential crack at surface point B. At CL1 during Transient 14, $K_{IB,\max}$ starts at approximately 8 MPa $m^{0.5}$ and increases to 57 MPa $m^{0.5}$. For Transient 2, it starts higher at about 31 MPa $m^{0.5}$ and rises to 240 MPa $m^{0.5}$, intersecting the K_{IC} master curve (solid green curve) in the *USE* region, suggesting failure at surface point B. At CL3 during Transients 2 and 14, $K_{IB,\max}$ begins at about 8 MPa $m^{0.5}$, reaching 61 MPa $m^{0.5}$ without irradiation embrittlement and 30 MPa $m^{0.5}$ when the impact of irradiation embrittlement is included. In both transients, $K_{IB,\max}$ at CL3 does not intersect the K_{IC} master curve, indicating failure is unlikely at surface points.

Analysis of the $K_{IA,\max}$ and $K_{IB,\max}$ values for initial crack depths a_0/t ranging from 5% to 80% reveals that without irradiation embrittlement the final K_I values converge to similar levels. This convergence happens because K_I evolutions for all considered a_0/t follow a similar trajectory. This behavior is attributed to the design loads for each transient in Service Level A remaining unchanged for every cycle, resulting in uniform stress responses under these conditions. As a result, K_I increases proportionally with crack depth (Equation (3) due to the unvarying application of these design loads. This means that, while initial crack depths a_0/t influence the initial K_I, they have limited impact on the final K_I, especially in unirradiated conditions. In contrast, irradiation embrittlement introduces variability in final K_I values due to time-dependent neutron fluence. This variability highlights the influence of

[5] As shown in Table 1, Transient 2 consists of two sub-transients. Sub-transient 2a covers the heat-up period, when the reactor is brought from a shutdown state to its normal operating pressure and temperature. Sub-transient 2b covers the cool-down period, when the reactor is taken from normal operating conditions back down to shutdown state.

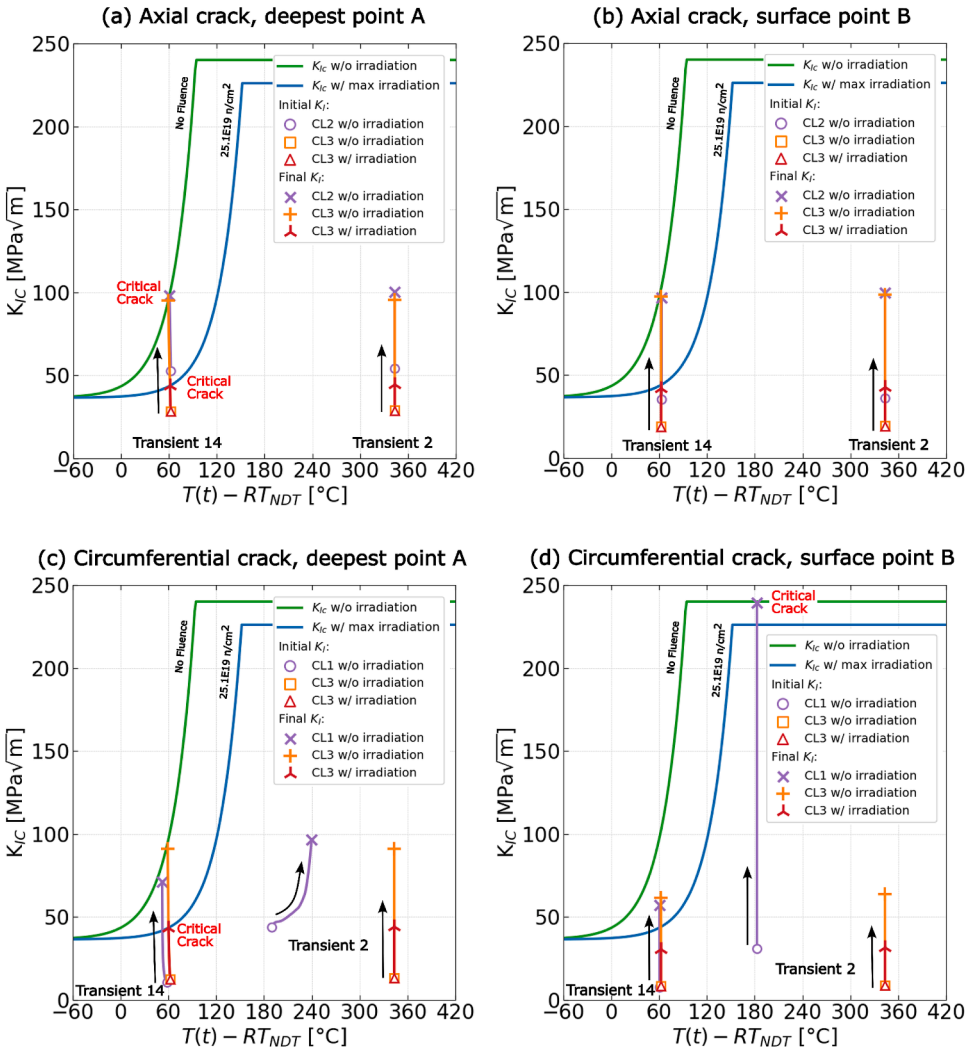

Fig. 9. SIF evolution from an initial 5% through-wall crack depth until failure for axial and circumferential cracks at the deepest and surface points.

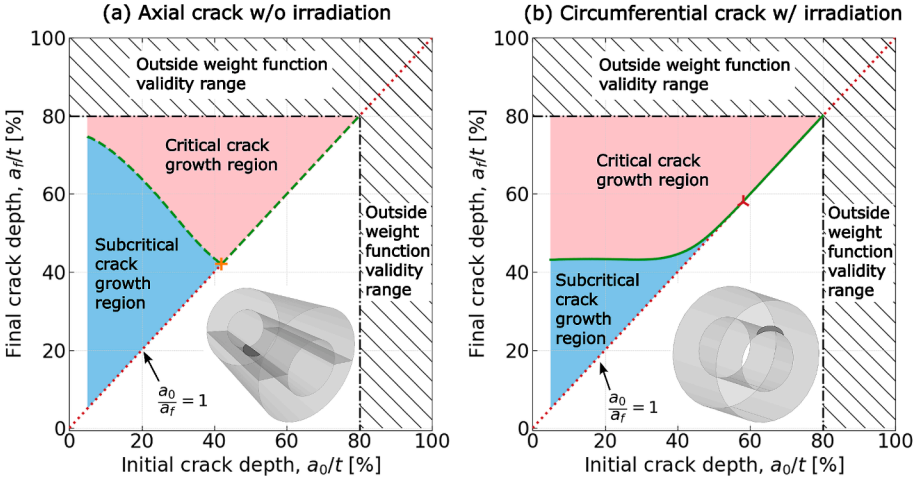

Fig. 10. Final crack depths at failure for initial depths from 5% to 80% of the wall thickness in the beltline region CL3, highlighting critical and subcritical crack growth regions for (a) axial cracks without irradiation and (b) circumferential cracks with irradiation. The cylinder thicknesses are exaggerated for illustration.

irradiation embrittlement, operational stresses, and crack geometry on K_I evolution, which directly affects FCG (discussed in Section 3.3).

3.3. Fatigue crack growth analysis

The SIF range ΔK_I, derived from the stress range $\Delta\sigma$, was used to calculate FCG rates in accordance with ASME Code Section XI, Article A-4000 (ASME, 2019). These FCG rates form the basis for determining the crack growth history, which was calculated using the methodology outlined in the flowchart in Fig. 5. This crack growth history offers insight into how cracks of different orientations, such as axial and circumferential, evolve under varying stress conditions.

To illustrate these insights, Fig. 10 presents examples of final crack depths a_f/t, derived from the crack growth history, focusing on subcritical and critical growth regions. For axial cracks, Fig. 10a shows the evolution of a_f/t for a range of initial crack depth ratios a_0/t from 5% to 80% of the wall thickness, in increments of 0.1%, specifically for the beltline region CL3 without irradiation embrittlement. Notably, an initial crack depth ratio a_0/t of 5% results in a final crack depth of 75%, corresponding to a $K_{IA,\max}$ of 95 MPa m$^{0.5}$ at CL3, as shown in Fig. 9a. As a_0/t increases, initial axial cracks become critical at shallower depths, with a turning point around 42% through the wall, as marked in Fig. 10a. Beyond this depth, cracks transition into critical growth. These transitions are depicted in the figure: the blue region represents subcritical growth, where cracks propagate stably, while the pink region indicates critical growth, leading to full wall penetration. The hatched area represents the upper validity limit of the weight function method, restricting further analysis of crack behavior.

When it comes to circumferential cracks, Fig. 10b examines crack growth at CL3 under irradiation embrittlement. For an initial a_0/t of 5%, the final depth reaches 43%, corresponding to a $K_{IA,\max}$ of 43 MPa m$^{0.5}$, as shown in Fig. 9c. Unlike axial cracks, circumferential cracks maintain relatively stable depths as a_0/t increases, up to 58% through-wall, as marked in Fig. 10b. Beyond this threshold, circumferential cracks also transition into critical growth. The blue and pink regions in the figure similarly represent subcritical and critical growth, respectively. A key observation from comparing axial and circumferential cracks at CL3 is that unirradiated axial cracks propagate deeper than irradiated circumferential cracks. This difference arises from the higher fracture toughness of unirradiated axial cracks, as shown in Fig. 9a and c.

To expand on these observations, Fig. 11 compares the final depths of axial and circumferential cracks under both irradiated and unirradiated conditions. Fig. 11a focuses on axial cracks. Without irradiation embrittlement, an initial a_0/t of 5% results in final crack depths of 28% at the inlet nozzle CL2 (dashed blue curve) and 75% at the beltline CL3 (dashed green curve). These correspond to $K_{IA,\max}$ of 98 MPa m$^{0.5}$ and 95 MPa m$^{0.5}$, respectively, at the deepest point A during Transient 14, as shown in Fig. 9a. As the initial crack depth increases to a critical level, the final depths reduce to 19% at CL2 and 42% at CL3, as marked in Fig. 11a. When irradiation embrittlement is introduced, the final fracture response is severely limited. For an initial a_0/t of 5%, the final crack depth at CL3 drops from 75% to 18% (solid green curve), corresponding to a $K_{IA,\max}$ of 44 MPa m$^{0.5}$, as shown in Fig. 9a. Notably, the final critical crack depth at CL3 becomes similar to that at CL2, approximately 19%, as marked in Fig. 11a. These findings emphasize the pronounced effect that irradiation embrittlement has on accelerating the transition of axial crack growth from the subcritical to the critical region, especially in the beltline region CL3.

Fig. 11b highlights the behavior of circumferential cracks. Without irradiation embrittlement, an initial a_0/t of 5% produces a final a_f/t of 78% at the outlet nozzle CL1 (dashed blue curve), with the critical initial crack depth reaching 80% (the upper validity limit of the weight function method), as marked in the figure. At this location, the corresponding $K_{IB,\max}$ is 240 MPa m$^{0.5}$ at the surface point B during Transient 2, as shown in Fig. 9d. With irradiation embrittlement, the final a_f/t for the same initial a_0/t drops to 43% at CL3 (solid green curve), corresponding to a $K_{IA,\max}$ of 43 MPa m$^{0.5}$ at the deepest point A during Transient 14, as shown in Fig. 9c. At critical initial depth, the final a_f/t at CL3 increases to 58%, as marked in Fig. 11b. Note that circumferential crack results without irradiation embrittlement are not reported because the analysis reaches the upper limit of the weight function method without crossing the K_{IC} master curve. This suggests that circumferential cracks without irradiation embrittlement at CL3 could potentially grow deeper if a weight function valid for longer cracks were available. These observations indicate that, in the beltline region CL3, irradiation embrittlement prompts an earlier progression of circumferential crack growth from subcritical to critical behavior.

To further analyze crack behavior, Fig. 12 explores the final aspect ratios a_f/c_f of axial and circumferential cracks across a range of initial crack depths, illustrating the impact of crack orientation and irradiation embrittlement on crack shape evolution. Fig. 12a focuses on axial cracks. Without irradiation embrittlement, axial cracks tend to grow deeper rather than wider. For an initial a_0/t of 5%, the aspect ratio at CL2 increases from 33% to 59% (dashed blue curve), elongating the axial crack along the depth direction. At CL3, axial cracks grow even more extensively in depth, with the aspect ratio increasing to 82% (dashed green curve). With irradiation embrittlement, the final aspect ratio at CL3 decreases to 72% (solid green curve), though it remains

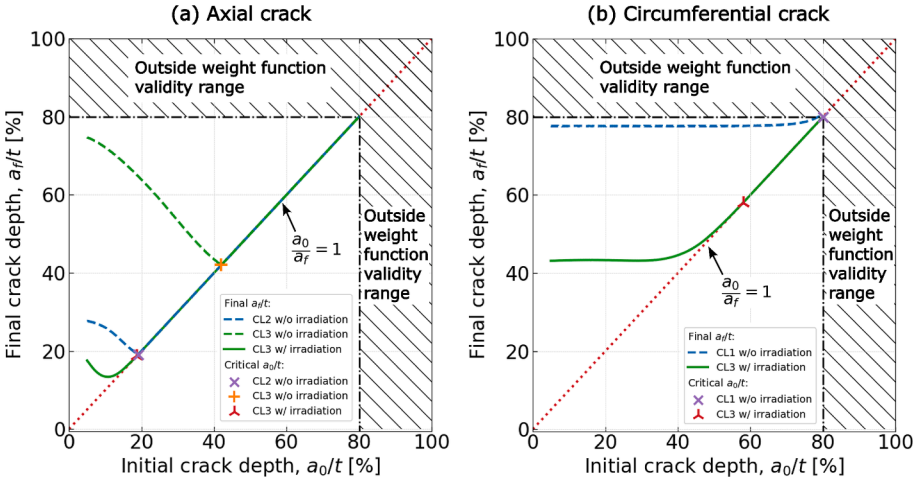

Fig. 11. Final crack depths before failure for initial depths ranging from 5% to 80% of the wall thickness: (a) axial cracks and (b) circumferential cracks.

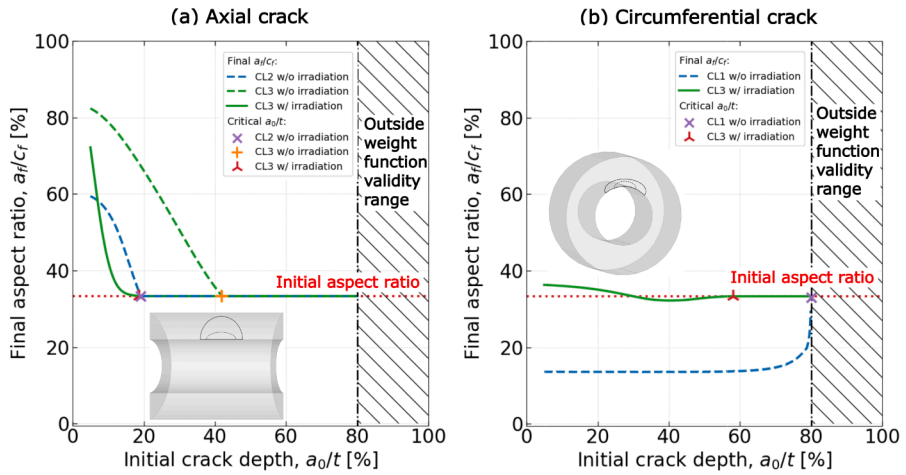

Fig. 12. Final aspect ratios before failure for initial depths ranging from 5% to 80% of the wall thickness: (a) axial cracks and (b) circumferential cracks.

higher than a_f/c_f at CL2. As a_0/t increases, final aspect ratios for axial cracks converge toward their initial values at the same critical initial depths as those shown in Fig. 11a, where critical crack growth occurs. Fig. 12b highlights the growth characteristics of circumferential cracks. Without irradiation embrittlement, circumferential cracks at CL1 primarily grow in length, reaching a final a_f/c_f of 14%, which remains consistent across deeper initial cracks. At CL3, circumferential cracks maintain an aspect ratio close to their initial value of 33%, with minimal variation. Similar to axial cracks, final aspect ratios for circumferential cracks converge toward their initial values at the same critical initial depths as those shown in Fig. 11b, where critical crack growth occurs.

Figs. 11 and 12 show the impact of irradiation embrittlement, crack orientation, and crack location on FCG behaviors, which play a critical role in determining the fatigue life of the RPV. Axial cracks predominantly grow deeper, particularly in the beltline region CL3, while circumferential cracks predominantly grow longer, especially at the outlet nozzle CL1. Despite these differences in growth behavior, both crack orientations tend to converge toward their initial aspect ratios as initial crack depths increase. These crack growth patterns and final fracture responses underscore the influence that initial crack geometry has on the fatigue life of the RPV, which is discussed Section 3.4.

3.4. Fatigue life analysis

Neutron irradiation embrittlement is a critical factor that can significantly limit the service life of RPVs in nuclear power plants. Fig. 13 illustrates its impact on fatigue life for initial a_0/t ranging from 5% to 80%, focusing on axial and circumferential cracks. Fatigue life predictions were calculated using the Paris equation (Equation (11)) under both irradiated and unirradiated conditions. The dashed lines in the figure represent fatigue life without irradiation, while the solid lines show the reduced fatigue life when irradiation is considered. Markers at the bottom of the figure indicate critical initial crack depths, where fracture toughness is reached immediately upon initiation, resulting in failure. The hatched region highlights areas beyond the upper validity range of the weight function used in the analysis.

Fig. 13a presents fatigue life predictions for axial cracks, comparing the effects of irradiation embrittlement in the inlet nozzle corner CL2 and the beltline region CL3. At CL2 without irradiation, fatigue life predictions (dashed blue curve) indicate a limiting initial a_0/t of 14% at around 100 years. At this depth, the crack becomes critical at approximately 19%, as shown in the figure. Beyond this depth, any initiating crack leads to immediate failure. At CL3, where neutron fluence is the highest, the impact of irradiation embrittlement is pronounced. Without irradiation, the fatigue life prediction (dashed green curve) at 100 years

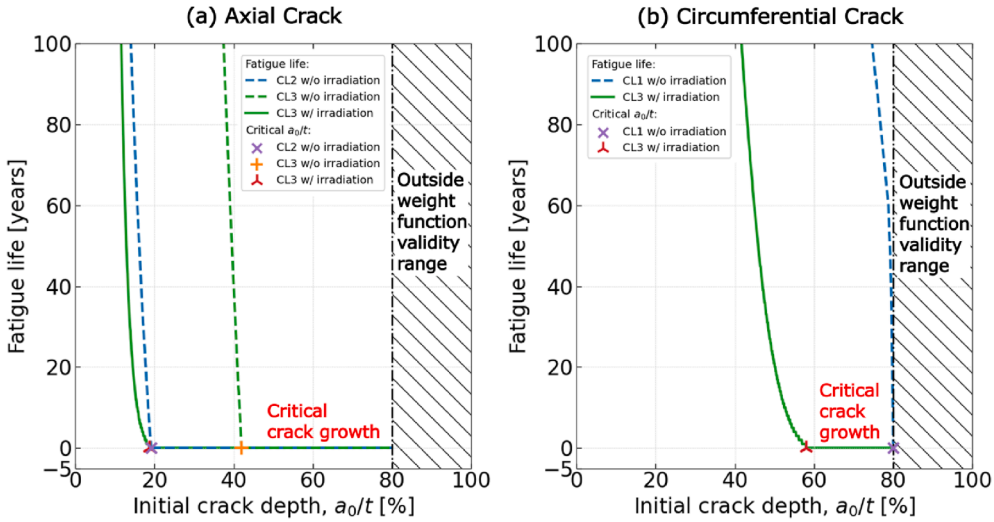

Fig. 13. Fatigue life with and without irradiation embrittlement for initial depths ranging from 5% to 80% of the wall thickness: (a) axial cracks and (b) circumferential cracks.

corresponds to a limiting initial a_0/t of 37%, with critical crack growth occurring at 42%. When irradiation embrittlement is considered, fatigue life is dramatically reduced (solid green curve). At 100 years, the limiting initial a_0/t decreases to 12%, with critical crack growth occurring at 19%. This highlights how irradiation embrittlement severe reduces fatigue life for axial cracks in the beltline region CL3.

Fig. 13b presents fatigue life predictions for circumferential cracks, providing fatigue life predictions for the outlet nozzle corner CL1 and the beltline region CL3. At CL1 without irradiation, fatigue life predictions (dashed blue curve) at 100 years indicate a limiting initial crack depth of 75%. As the initial crack depth increases, fatigue life decreases, with the critical initial crack depth reaching 80% through-wall (the upper validity limit of the weight function). At CL3, circumferential crack behavior is markedly different due to irradiation embrittlement. Without irradiation, the analysis reaches the upper validity limit of the weight function at 80% through-wall without showing critical crack growth, so fatigue life predictions for this case are excluded from the figure. With irradiation (solid green curve), fatigue life is significantly reduced. At 100 years, the limiting initial a_0/t decreases to 42%, with critical crack growth occurring at 58%. Beyond this point, further crack growth leads to failure. These results demonstrate the pronounced impact of irradiation embrittlement on circumferential cracks in high-fluence regions such as the beltline.

Fig. 13 illustrates the substantial impact of irradiation embrittlement on fatigue life, particularly in regions exposed to high neutron fluence such as the beltline region CL3. In this region, the fatigue life of both axial and circumferential cracks is markedly reduced compared to that of unirradiated conditions, emphasizing the critical role of neutron exposure in accelerating structural degradation. Despite this, circumferential cracks in the outlet nozzle region CL1 exhibit relatively long fatigue lives, highlighting the varying sensitivity of different regions and crack orientations to irradiation effects. This observation underscores the importance of considering location-specific factors when assessing RPV integrity.

4. Conclusion

In this study, we conducted a detailed thermo-mechanical stress analysis of a representative reactor pressure vessel under Service Level A transients to evaluate fatigue crack growth behavior and its implication for fitness-for-service assessment. The performed thermo-mechanical numerical analysis identified three critical locations: the outlet nozzle corner (CL1), the inlet nozzle corner (CL2), and the beltline region (CL3). CL1 and CL2 were identified as critical due to high operational stresses in these regions, while CL3 was considered critical because of its proximity to the reactor core and exposure to high neutron fluence, which leads to irradiation embrittlement of the pressure vessel material.

Using linear elastic fracture mechanics, an algorithm was developed to evaluate the fatigue crack growth behavior for all Service Level A transients for crack depth ratios a_0/t ranging from 5% to 80%. Two most severe Service Level A transients (Transients 2 and 14) were selected to illustrate SIF evolution for axial and circumferential cracks at both the deepest and surface points of the identified critical locations. Final fracture responses, including crack depths and aspect ratios, were assessed under irradiated and unirradiated conditions using the aforementioned algorithm. Additionally, fatigue life predictions were presented, with a focus on the effects of neutron irradiation embrittlement.

The performed analysis reveals that fatigue life is dependent on the combination of the magnitude of extreme operational stresses ($\Delta\sigma = \sigma_{max} - \sigma_{min}$) and the extent of the impact of neutron irradiation on the fracture toughness of the material. Without consideration of material embrittlement due to radiation, we found that the axial cracks at the inlet nozzle (CL2) most significantly limited the fatigue life of the reactor pressure vessel. The neutron flux above the beltline region is insufficient to cause significant material embrittlement; however, other material-property-altering mechanisms, such as long-term aging, might need to be considered in future analysis. When irradiation embrittlement is considered, axial cracks in the beltline region (CL3) became the most life limiting due to the reduction in fracture toughness caused by the high neutron fluence in this region. However, the current analysis considers the neutron fluence of 25.1E19 n/cm^2, which is expected to cause the maximum drop in the fracture toughness and is unlikely to be seen in the operation.

The performed analysis also shows that axial cracks are generally more life limiting than circumferential cracks, particularly at CL2 and CL3. These distinctions underscore the importance of accounting for crack orientation and location when developing fitness-for-service assessments. Furthermore, it was found that failures were more likely to occur at lower temperatures within the brittle regime, where reduced fracture toughness limits the material's ability to resist crack propagation under cyclic loading. This behavior was particularly evident during low-temperature conditions, such as those encountered during leakage tests (Transient 14). Such conditions provide opportunities to detect and mitigate cracks before a reactor returns to full operation.

The sensitivity of fatigue crack growth to neutron flux and temperature highlights the need to assess RPVs across a range of operational conditions. Accounting for these operational factors is essential for ensuring the safe and reliable operation of nuclear power plants over extended service periods.

CRediT authorship contribution statement

M.N. Tran: Visualization, Investigation, Writing – original draft, Methodology, Software, Formal analysis, Writing – review & editing, Conceptualization. **O. Muránsky:** Investigation, Visualization, Writing – review & editing, Project administration. **B.W. Spencer:** Software, Supervision, Methodology, Writing – review & editing.

Declaration of competing interest

The authors declare that they have no known competing financial interests or personal relationships that could have appeared to influence the work reported in this paper.

Acknowledgements

The authors gratefully acknowledge the support provided by the Australian Nuclear Science and Technology Organisation (ANSTO) and Idaho National Laboratory (INL). The work of Tran and Muransky was supported by the Australian Government through ANSTO's internal funding, including access to ANSTO's high-performance computing infrastructure. The work of Spencer was supported by Battelle Energy Alliance, LLC under contract no. DE-AC07-05ID14517 with the U.S. Department of Energy.

Appendix

Table A1
Calculated applied internal pressure and far-field temperature from the design transients, and their resulting applied end-cap pressure and internal heat transfer coefficients.

			RPV			Inlet Nozzles		Outlet Nozzles		Injection Nozzles			
Event	Cycles per Year	Time (sec)	Temp (K)	Pressure (MPa)	h (W/mm^2·K)	End-Cap Pressure (MPa)	h (W/mm^2·K)	End-Cap Pressure (MPa)	h (W/mm^2·K)	Temp (K)	Pressure (MPa)	End-Cap Pressure (MPa)	h (W/mm^2·K)
1a	3.33	0	294.26	0.00	1.09E-04	0.00	1.78E-04	0.00	1.63E-04	294.26	0.00	0.00	9.20E-07
		1800	294.26	2.76	1.75E-03	5.31	1.89E-02	5.95	1.78E-02	294.26	0.00	0.00	9.20E-07
1b	3.33	0	294.26	0.00	1.09E-04	0.00	1.78E-04	0.00	1.63E-04	294.26	0.00	0.00	9.20E-07
		1800	294.26	2.76	1.75E-03	5.31	1.89E-02	5.95	1.78E-02	294.26	0.00	0.00	9.20E-07
		3600	294.26	0.00	1.09E-04	0.00	1.78E-04	0.00	1.63E-04	294.26	0.00	0.00	9.20E-07
1c	6.67	0	294.26	0.00	1.09E-04	0.00	1.78E-04	0.00	1.63E-04	294.26	0.00	0.00	9.20E-07
		1080	310.93	2.76	2.05E-03	5.31	2.22E-02	5.95	2.08E-02	310.93	0.00	0.00	4.31E-05
		2160	294.26	0.00	1.09E-04	0.00	1.78E-04	0.00	1.63E-04	294.26	0.00	0.00	9.20E-07
1d	36.67	0	564.82	15.41	3.61E-03	29.67	3.90E-02	33.26	3.67E-02	335.93	0.00	0.00	4.12E-05
		3600	564.82	15.24	3.60E-03	29.34	3.90E-02	32.89	3.67E-02	335.93	0.00	0.00	4.12E-05
		7200	564.82	15.41	3.61E-03	29.67	3.90E-02	33.26	3.67E-02	335.93	0.00	0.00	4.12E-05
2a	3.33	0	294.26	0.00	1.09E-04	0.00	1.78E-04	0.00	1.63E-04	294.26	0.00	0.00	9.20E-07
		2700	335.93	0.00	1.75E-04	0.00	2.83E-04	0.00	2.60E-04	335.93	0.00	0.00	4.12E-05
		5400	335.93	4.27	2.37E-03	8.23	2.57E-02	9.23	2.41E-02	335.93	0.00	0.00	4.12E-05
		6300	349.82	4.27	2.64E-03	8.23	2.86E-02	9.23	2.68E-02	335.93	0.00	0.00	4.12E-05
		8100	349.82	6.89	2.64E-03	13.27	2.86E-02	14.88	2.69E-02	335.93	0.00	0.00	4.12E-05
		25,380	616.48	17.13	2.38E-03	32.99	2.57E-02	36.98	2.42E-02	335.93	0.00	0.00	4.12E-05
		54,180	616.48	17.13	2.38E-03	32.99	2.57E-02	36.98	2.42E-02	335.93	0.00	0.00	4.12E-05
2b	3.33	0	616.48	17.13	2.38E-03	32.99	2.57E-02	36.98	2.42E-02	335.93	0.00	0.00	4.12E-05
		10,800	449.82	12.38	3.62E-03	23.83	3.92E-02	26.71	3.68E-02	335.93	0.00	0.00	4.12E-05
		27,000	324.82	0.00	1.61E-04	0.00	2.61E-04	0.00	2.39E-04	324.82	0.00	0.00	4.20E-05
		55,800	294.26	0.00	1.09E-04	0.00	1.78E-04	0.00	1.63E-04	294.26	0.00	0.00	9.20E-07
3a	8.33	0	449.82	6.89	3.61E-03	13.27	3.91E-02	14.88	3.67E-02	335.93	0.00	0.00	4.12E-05
		7200	564.82	15.24	3.60E-03	29.34	3.90E-02	32.89	3.67E-02	335.93	0.00	0.00	4.12E-05
		9000	572.57	15.52	3.55E-03	29.88	3.85E-02	33.50	3.61E-02	335.93	0.00	0.00	4.12E-05
3b	8.33	0	572.57	15.52	3.55E-03	29.88	3.85E-02	33.50	3.61E-02	335.93	0.00	0.00	4.12E-05
		300	564.82	15.24	3.60E-03	29.34	3.90E-02	32.89	3.67E-02	335.93	0.00	0.00	4.12E-05
4a	33.33	0	572.57	15.52	3.55E-03	29.88	3.85E-02	33.50	3.61E-02	335.93	0.00	0.00	4.12E-05
		1020	616.48	17.13	2.38E-03	32.99	2.57E-02	36.98	2.42E-02	335.93	0.00	0.00	4.12E-05
4b	33.33	0	616.48	17.13	2.38E-03	32.99	2.57E-02	36.98	2.42E-02	335.93	0.00	0.00	4.12E-05
		1020	572.57	15.52	3.55E-03	29.88	3.85E-02	33.50	3.61E-02	335.93	0.00	0.00	4.12E-05
5a	50.00	0	572.57	15.52	3.55E-03	29.88	3.85E-02	33.50	3.61E-02	335.93	0.00	0.00	4.12E-05
		2845.8	616.48	17.13	2.38E-03	32.99	2.57E-02	36.98	2.42E-02	335.93	0.00	0.00	4.12E-05
5b	50.00	0	616.48	17.13	2.38E-03	32.99	2.57E-02	36.98	2.42E-02	335.93	0.00	0.00	4.12E-05
		2845.8	572.57	15.52	3.55E-03	29.88	3.85E-02	33.50	3.61E-02	335.93	0.00	0.00	4.12E-05
6	3.33	0	616.48	17.13	2.38E-03	32.99	2.57E-02	36.98	2.42E-02	335.93	0.00	0.00	4.12E-05
		900	595.82	16.38	3.03E-03	31.53	3.29E-02	35.34	3.09E-02	335.93	0.00	0.00	4.12E-05
7ai	1250.00	0	616.48	17.13	2.38E-03	32.99	2.57E-02	36.98	2.42E-02	335.93	0.00	0.00	4.12E-05
		60	614.82	16.96	2.43E-03	32.65	2.63E-02	36.61	2.47E-02	335.93	0.00	0.00	4.12E-05
		120	616.48	17.13	2.38E-03	32.99	2.57E-02	36.98	2.42E-02	335.93	0.00	0.00	4.12E-05
7aii	1250.00	0	616.48	17.13	2.38E-03	32.99	2.57E-02	36.98	2.42E-02	335.93	0.00	0.00	4.12E-05
		60	618.15	17.31	2.33E-03	33.32	2.53E-02	37.35	2.37E-02	335.93	0.00	0.00	4.12E-05
		120	616.48	17.13	2.38E-03	32.99	2.57E-02	36.98	2.42E-02	335.93	0.00	0.00	4.12E-05
7bi	38333.33	0	616.48	17.13	2.38E-03	32.99	2.57E-02	36.98	2.42E-02	335.93	0.00	0.00	4.12E-05
		180	616.21	17.09	2.38E-03	32.91	2.58E-02	36.89	2.42E-02	335.93	0.00	0.00	4.12E-05
		360	616.48	17.13	2.38E-03	32.99	2.57E-02	36.98	2.42E-02	335.93	0.00	0.00	4.12E-05
7bii	38333.33	0	616.48	17.13	2.38E-03	32.99	2.57E-02	36.98	2.42E-02	335.93	0.00	0.00	4.12E-05
		180	616.76	17.17	2.38E-03	33.07	2.57E-02	37.07	2.42E-02	335.93	0.00	0.00	4.12E-05
		360	616.48	17.13	2.38E-03	32.99	2.57E-02	36.98	2.42E-02	335.93	0.00	0.00	4.12E-05
7c	12500.00	0	616.48	17.04	2.33E-03	32.80	2.53E-02	36.78	2.37E-02	335.93	0.00	0.00	4.12E-05
		60	616.48	17.00	2.32E-03	32.73	2.51E-02	36.69	2.36E-02	335.93	0.00	0.00	4.12E-05
		120	616.48	16.96	2.30E-03	32.66	2.49E-02	36.61	2.34E-02	335.93	0.00	0.00	4.12E-05
		180	616.48	16.92	2.28E-03	32.59	2.47E-02	36.53	2.32E-02	335.93	0.00	0.00	4.12E-05
		240	616.48	16.89	2.27E-03	32.51	2.45E-02	36.45	2.30E-02	335.93	0.00	0.00	4.12E-05
		300	616.48	16.85	2.25E-03	32.44	2.44E-02	36.37	2.29E-02	335.93	0.00	0.00	4.12E-05
		360	616.48	16.89	2.27E-03	32.51	2.45E-02	36.45	2.30E-02	335.93	0.00	0.00	4.12E-05
		420	616.48	16.92	2.28E-03	32.59	2.47E-02	36.53	2.32E-02	335.93	0.00	0.00	4.12E-05
		480	616.48	16.96	2.30E-03	32.66	2.49E-02	36.61	2.34E-02	335.93	0.00	0.00	4.12E-05
		540	616.48	17.00	2.32E-03	32.73	2.51E-02	36.69	2.36E-02	335.93	0.00	0.00	4.12E-05
		600	616.48	17.04	2.33E-03	32.80	2.53E-02	36.78	2.37E-02	335.93	0.00	0.00	4.12E-05
8	48.33	0	574.21	15.58	3.53E-03	30.00	3.83E-02	33.63	3.59E-02	335.93	0.00	0.00	4.12E-05
		1800	575.53	15.63	3.51E-03	30.09	3.80E-02	33.74	3.57E-02	335.93	0.00	0.00	4.12E-05
		3600	572.33	15.51	3.55E-03	29.87	3.85E-02	33.48	3.62E-02	335.93	0.00	0.00	4.12E-05
9a	50.00	0	616.48	17.13	2.38E-03	32.99	2.57E-02	36.98	2.42E-02	335.93	0.00	0.00	4.12E-05
		7200	564.82	15.41	3.61E-03	29.67	3.90E-02	33.26	3.67E-02	335.93	0.00	0.00	4.12E-05
		14,400	616.48	17.13	2.38E-03	32.99	2.57E-02	36.98	2.42E-02	335.93	0.00	0.00	4.12E-05

(*continued on next page*)

Table A1 (*continued*)

Event	Cycles per Year	Time (sec)	RPV			Inlet Nozzles		Outlet Nozzles		Injection Nozzles			
			Temp (K)	Pressure (MPa)	h (W/mm^2·K)	End-Cap Pressure (MPa)	h (W/mm^2·K)	End-Cap Pressure (MPa)	h (W/mm^2·K)	Temp (K)	Pressure (MPa)	End-Cap Pressure (MPa)	h (W/mm^2·K)
9b	250.00	0	616.48	17.13	2.38E-03	32.99	2.57E-02	36.98	2.42E-02	335.93	0.00	0.00	4.12E-05
		1440	564.82	15.41	3.61E-03	29.67	3.90E-02	33.26	3.67E-02	335.93	0.00	0.00	4.12E-05
		2880	616.48	17.13	2.38E-03	32.99	2.57E-02	36.98	2.42E-02	335.93	0.00	0.00	4.12E-05
10	0.67	0	616.48	17.13	2.38E-03	32.99	2.57E-02	36.98	2.42E-02	335.93	0.00	0.00	4.12E-05
		3600	564.82	15.24	3.60E-03	29.34	3.90E-02	32.89	3.67E-02	335.93	0.00	0.00	4.12E-05
11	3.00	0	616.48	17.13	2.38E-03	32.99	2.57E-02	36.98	2.42E-02	335.93	0.00	0.00	4.12E-05
		600	616.48	15.24	1.45E-03	29.34	1.57E-02	32.89	1.48E-02	335.93	0.00	0.00	4.12E-05
12	0.67	0	333.15	0.00	1.71E-04	0.00	2.78E-04	0.00	2.55E-04	333.15	0.00	0.00	4.14E-05
		2520	294.26	0.00	1.09E-04	0.00	1.78E-04	14.88	1.63E-04	294.26	6.89	11.42	2.40E-02
		13,320	294.26	0.00	1.09E-04	0.00	1.78E-04	14.88	1.63E-04	294.26	6.89	11.42	2.40E-02
13	0.33	0	449.82	6.89	3.61E-03	13.27	3.91E-02	14.88	3.67E-02	335.93	0.00	0.00	4.12E-05
		7452	564.82	15.24	3.60E-03	29.34	3.90E-02	32.89	3.67E-02	335.93	0.00	0.00	4.12E-05
		10,800	616.48	17.13	2.38E-03	32.99	2.57E-02	36.98	2.42E-02	335.93	0.00	0.00	4.12E-05
		21,600	449.82	6.89	3.61E-03	13.27	3.91E-02	14.88	3.67E-02	335.93	0.00	0.00	4.12E-05
14	3.33	0	324.82	0.00	1.61E-04	0.00	2.61E-04	0.00	2.39E-04	324.82	0.00	0.00	4.20E-05
		720	335.93	17.24	2.49E-03	33.19	2.69E-02	37.20	2.53E-02	335.93	0.00	0.00	4.12E-05
		4320	335.93	17.24	2.49E-03	33.19	2.69E-02	37.20	2.53E-02	335.93	0.00	0.00	4.12E-05
15	N/A		N/A			N/A		N/A		N/A			
16	0.08	0	564.82	15.41	3.61E-03	29.67	3.90E-02	33.26	3.67E-02	294.26	15.41	25.53	2.42E-02
		5652	477.59	15.41	3.69E-03	29.67	4.00E-02	33.26	3.76E-02	294.26	15.41	25.53	2.42E-02
		10,800	477.59	15.41	3.69E-03	29.67	4.00E-02	33.26	3.76E-02	294.26	15.41	25.53	2.42E-02
17	0.08	0	449.82	6.89	3.61E-03	13.27	3.91E-02	14.88	3.67E-02	335.93	0.00	0.00	4.12E-05
		1800	422.04	6.89	3.42E-03	13.27	3.70E-02	14.88	3.47E-02	335.93	0.00	0.00	4.12E-05
18	47.00	0	616.48	17.13	2.38E-03	32.99	2.57E-02	36.98	2.42E-02	335.93	0.00	0.00	4.12E-05
		28,800	616.48	15.24	1.45E-03	29.34	1.57E-02	32.89	1.48E-02	335.93	0.00	0.00	4.12E-05
		32,400	616.48	17.13	2.38E-03	32.99	2.57E-02	36.98	2.42E-02	335.93	0.00	0.00	4.12E-05
19	296.67	0	616.48	17.13	2.38E-03	32.99	2.57E-02	36.98	2.42E-02	335.93	0.00	0.00	4.12E-05
		28,800	590.65	16.19	3.17E-03	31.16	3.44E-02	34.93	3.23E-02	335.93	0.00	0.00	4.12E-05
		86,400	616.48	17.13	2.38E-03	32.99	2.57E-02	36.98	2.42E-02	335.93	0.00	0.00	4.12E-05

Data availability

Data will be made available on request.

References

ASME, 2019. ASME Boiler and Pressure Vessel Code, Section XI, Division 1, Rules for Inservice Inspection of Nuclear Power Plant Components. ASME BPVC.XI.1 - 2019.

Bai, X.-M., Ke, H., Zhang, Y., Spencer, B.W., 2017. Modeling copper precipitation hardening and embrittlement in a dilute Fe-0.3at.%Cu alloy under neutron irradiation. J. Nucl. Mater. 495, 442–454. https://doi.org/10.1016/j.jnucmat.2017.08.042.

Barsom, J., Rolfe, S., 1999. *Fracture and Fatigue Control in Structures: applications of Fracture Mechanics*. ASTM International.

US Nuclear Regulatory Commission, 1988. Regulatory Guide, Regulatory Guide 1.99, Rev. 2, May 1988. Radiation embrittlement of reactor vessel materials.

ASTM E185, 1998. Standard Practice for Conducting Surveillance Tests for Light-Water Cooled Nuclear Power Reactor Vessels, ASTM International, approved Jan. 10.

BlackBear Source Code Repository, https://github.com/idaholab/blackbear.

Bueckner, H.F., 1970. Novel principle for the computation of stress intensity factors. Z. Angew. Math. Mech. 50 (9), 529–546.

Choi, S., Surh, H.-B., Kim, J.-W., 2019. Effect of postulated crack location on the pressure-temperature limit curve of reactor pressure vessel. Nucl. Eng. Technol. 51 (6), 1681–1688. https://doi.org/10.1016/j.net.2019.05.004.

Coreform Cubit (Version 2024.3) [Computer software]. Orem, UT: Coreform LLC. Retrieved from http://coreform.com.

Dowling, N.E., 2013. Mechanical Behavior of Materials: Engineering Methods for Deformation, Fracture, and Fatigue, 4th ed. Pearson (in English), Boston.

Eason, E.D., Odette, G.R., Nanstad, R.K., Yamamoto, T., 2013. A physically-based correlation of irradiation-induced transition temperature shifts for RPV steels. J. Nucl. Mater. 433 (1), 240–254. https://doi.org/10.1016/j.jnucmat.2012.09.012.

Holman, J.P., 2010. *Heat transfer*, 10th ed. McGraw-Hill Education.

International Atomic Energy Agency, 2005b. Effects of Nickel on Irradiation Embrittlement. In: of Light Water Reactor Pressure Vessel Steels. IAEA, Vienna.

Westinghouse Electric Company, 2011. Westinghouse AP1000 Design Control Document, Revision 19, June 2011. [Online]. Available: https://www.nrc.gov/docs/ml1117/ml11171a500.html.

International Atomic Energy Agency, 2023. Fatigue Assessment in Light Water Reactors for Long Term Operation: Good Practices and Lessons Learned. IAEA,Vienna.

International Atomic Energy Agency, 2009a. Integrity of Reactor Pressure Vessels in Nuclear Power Plants: Assessment of Irradiation Embrittlement Effects in Reactor Pressure Vessel Steels. IAEA, Vienna.

International Atomic Energy Agency, 2009b. Master Curve Approach to Monitor Fracture Toughness of Reactor Pressure Vessels in Nuclear Power Plants. IAEA, Vienna.

Jiang, W., et al., 2024. Comparison of PM-HIP to forged SA508 pressure vessel steel under high-dose neutron irradiation. J. Nucl. Mater. 594, 155018. https://doi.org/10.1016/j.jnucmat.2024.155018.

Lindsay, A.D., et al., 2022. 2.0 - MOOSE: Enabling massively parallel multiphysics simulation. SoftwareX 20, 101202. https://doi.org/10.1016/j.softx.2022.101202.

International Atomic Energy Agency, 2005a. Guidelines for Application of the Master Curve Approach to Reactor Pressure Vessel Integrity in Nuclear Power Plants. IAEA, Vienna.

Muránsky, O., Smith, M.C., Bendeich, P.J., Edwards, L., 2011. Validated numerical analysis of residual stresses in Safety Relief Valve (SRV) nozzle mock-ups. Comput. Mater. Sci 50 (7), 2203–2215. https://doi.org/10.1016/j.commatsci.2011.02.031.

Odette, G.R., 1994. Radiation induced microstructural evolution in reactor pressure vessel steels. MRS Online Proc. Libr. 373 (1), 137–148. https://doi.org/10.1557/PROC-373-137.

US Nuclear Regulatory Commission, 2007. Standard Review Plan, NUREG-0800, Branch Technical Position 5-3, Rev. 2, March 2007. Fracture Toughness Requirements.

Eason, E.D., Wright, J.E., Odette, G.R., 1998. Improved embrittlement correlations for reactor pressure vessel steels. NUREG/CR-6551, MCS 970501, Nov, 1998.

Odette, G.R., Lucas, G.E., 2001. Embrittlement of nuclear reactor pressure vessels. JOM, 53(7), 18–22. [Online]. Available: https://link.springer.com/article/10.1007/s11837-001-0081-0.

Ortner, S., Styman, P.D., Long, E., 2024. The effects of flux on the radiation-induced embrittlement of reactor pressure vessel steels: review of current understanding and application to high fluences. Front. Nucl. Eng.

Paris, P., Erdogan, F., 1963. A critical analysis of crack propagation laws. J. Basic Eng. 85 (4), 528–533. https://doi.org/10.1115/1.3656900.

Rice, J.R., 1972. Some remarks on elastic crack-tip stress fields. Int. J. Solids Struct. 8 (6), 751–758. https://doi.org/10.1016/0020-7683(72)90040-6.

Juergen Riegel, Werner Mayer, Yorik van Havre, and others, 2001–2023. FreeCAD (Version 0.21.1). [Software] Available from http://www.freecadweb.org.
Rohsenow, W.M., Hartnett, J.P., Cho, Y.I., 1998. Handbook of Heat Transfer, 3rd ed. (McGraw-Hill handbooks). New York: McGraw-Hill (in English).
Spencer, B.W., Hoffman, W.M., Collins, B.S., Henderson, S.C., 2020. Coupling of Neutron Transport and Probabilistic Fracture Mechanics Codes for Analysis of Embrittled Reactor Pressure Vessels vol. 3. https://doi.org/10.1115/PVP2020-21680.
Terán, G., Capula-Colindres, S., Angeles-Herrera, D., Velázquez, J.C., Fernández-Cueto, M.J., 2016. Estimation of fracture toughness KIC from Charpy impact test data in T-welded connections repaired by grinding and wet welding. Eng. Fract. Mech. 153, 351–359. https://doi.org/10.1016/j.engfracmech.2015.12.010.
Tran, M.N., Muransky, O., Spencer, B.W., 2024. Fitness-for-service analysis of a light water reactor pressure vessel under complex operating conditions. In: ASME 2024 Pressure Vessels & Piping Conference, vol. 4: Materials & Fabrication, V004T06A032, doi: https://doi.org/10.1115/PVP2024-121895.
Wagner, W., Kretzschmar, H.-J., 2008. International Steam Tables: Properties of Water and Steam based on the Industrial Formulation IAPWS-IF97, 2nd ed.